Crack detection and localization in RC beams through smart MWCNT/epoxy strip-like strain sensors

Enrique García-Macías[a,*], Luis Rodríguez-Tembleque[a], Andrés Sáez[a], Filippo Ubertini[b]

[a]*Department of Continuum Mechanics and Structural Analysis, School of Engineering, Universidad de Sevilla, Spain*
[b]*Department of Civil and Environmental Engineering, University of Perugia, Via G Duranti 93, Perugia 06125, Italy*

Highlights

- A 3D FE simulation of MWCNT-reinforced smart strips is presented

- A multichannel measurement setup is incorporated in the numerical model

- An Euler-Bernoulli model of beams with smart strips is developed

- A damage identification algorithm is proposed for smart strips deployed on beam structures

Abstract

In recent years, self-sensing structural materials have drawn enormous attention of scientific community due to their potential to enable continuous monitoring of the integrity of structures. The new paradigm of smart condition-based maintenance advocates the use of next-generation structures completely or partly constituted by self-sensing materials, that is, the structure or part of it also behaves as a sensor. In this context, the remarkable mechanical and electrical properties of Multi Walled Carbon NanoTubes (MWCNTs) have fostered an increasing number of applications as fillers for composites with multifunctional properties. Among a wide spectrum of potential applications, the development of skin-type piezoresistive distributed strain sensors shows great promise. Such sensors can be deployed onto large-scale structures, enabling a continuous monitoring of the strain state in the global area of the structure. In this paper, a theoretical study on the potential application of smart MWCNT/epoxy strip-like strain sensors for damage detection/localization/quantification in Reinforced Concrete (RC) beams is presented. A micromechanics-based finite element model is proposed for the electromechanical analysis of MWCNT/epoxy strips. Furthermore, a damage detection algorithm through model updating approach is introduced. To do so, an Euler-Bernoulli model for beams equipped with a smart MWCNT/epoxy strip is developed. Finally, two numerical case studies are presented including: a 2D concrete beam with multiple prescribed crack-like damages, and a 3D RC beam under four-point flexural conditions with non-prescribed cracking. Results show that the proposed smart strips are capable of exploiting the damage-induced variations in the electrical output to locate and quantify damages for real-time distributed structural health monitoring of RC beam structures.

Keywords: Carbon nanotube, Micromechanics, Piezoresistivity, Damage detection, Sensor network, Structual Health Monitoring, Damage localization, Smart composite

---

1. Introduction

The enormous costs derived from run-to-failure maintenance of civil infrastructure have fostered outstanding advances in the realm of Structural Health Monitoring (SHM) in the last decades. In particular, there is a great concern about the lifespan of concrete structures because of their high material discreteness and vulnerability to ageing degradation [1]. Nonetheless, most off-the-shelf monitoring solutions, such as accelerometers or strain gauges, only provide quasi-point measurements and, thus, damages may be hard to detect if the sensors are not properly located [2]. Although some innovative technologies, such as fiber-optic sensors, offer distributed sensing capabilities [3, 4], these are hardly scalable to large-scale structures and long-term monitoring without incurring elevated costs and complex signal processing algorithms. The hasty growth of nanotechnologies has permitted the development of new multifunctional materials with a vast range of applications in many different fields of Structural Engineering. In particular, Multi-Walled Carbon NanoTube (MWCNT) based composites have

*Corresponding author.
Email address:* `egarcia28@us.es` (Enrique García-Macías)

attracted great interest due to their piezoresistive properties, that is to say, composites themselves behave as sensors through measurable variations of their electrical properties under mechanical deformations [5]. In this way, many researchers have striven to develop smart engineering materials for SHM applications, including cement-based composites [6, 7], smart polymeric materials [8, 9], or strain sensing bricks [10]. Notwithstanding great efforts on the development of pilot applications, there is not yet a well-established theoretical approach that allows for assisting the design and correctly interpreting the output of the sensors.

Many authors have striven to develop efficient solutions for SHM through smart structures with the ability to monitor their own condition [11]. In order to detect early stage damages, conduct preventive maintenance or estimate prognosis on certain damages, the deployment of such smart systems must be capable of damage diagnosis and localization [12]. A promising solution for local/global damage localization in civil infrastructure is the implementation of dense surface sensor networks, often termed sensing skins. Once deployed onto the structure, such systems permit the real-time condition assessment of the structural response over its global area, and the appearance of damages can be correlated to local perturbations in the response. Various researchers have proposed conductive surface sensors, whereby the appearance of cracks is manifested by local increases in the electrical resistance. It is worth noting the work by Hallaji and Pour-Ghaz [13] who developed a silver-based conductive paint for crack detection and localization in cement-based materials. Cracking in the substrate concrete was correlated to local variations in the electrical resistance of the sensing skin by Electrical Resistance Tomography (ERT). The so-called Large Area Electronics (LAE) offer another highly scalable sensing solution to form dense sensor networks. Yao and Glisic [14] proposed large sensing sheets of Resistive Strain Gauges (RSGs) patterned on a flexible polyimide substrate to cover large areas of structures. Similarly, Laflamme et al. [15] proposed the use of a hybrid dense sensor network consisting of large-area strain-sensing soft capacitive sensors for the low-cost monitoring of large structures.

Although the sensing solutions mentioned above are certainly promising, they lack the capability to directly detect damages that do not come into contact with the sensing skin such as internal damages. The implementation of multifunctional materials such as self-sensing piezoresistive composites offers an attractive alternative. Along these lines, three different integration alternatives of self-sensing composites into large-scale structures can be found in the literature: bulk smart materials, embedded sensors [16], and self-sensing strips [17]. The first group utilizes structural elements fully constituted by self-sensing materials. An illustrative example is the work by Howser *et al.* [18] who reported the fabrication of self-consolidating concrete doped with carbon nanofibers for crack detection in shear columns. Downey *et al.* [19] proposed a biphasic DC measurement approach for use in the resistance measurement of MWCNT-reinforced cement-based composite beams for damage detection and localization. Although the development of structures fully constituted by self-sensing composite provides a comprehensive monitoring of the global volume of the structure, the high costs of the nanoparticles and complex fabrication processes related to their dispersion place huge constraints on these solutions [20]. Alternatively, the application of smart composites in the shape of a dense network of embedded sensors offers a more cost-efficient solution. Naeem *et al.* [21] analyzed the stress and crack sensing capabilities of MWCNT/cement-based composites under flexural loadings. Those authors manufactured prismatic embeddable sensors with different geometries, including smart sensors of 50x50x50 mm^3, 160x40x40 mm^3 and 1500x15x15 mm^3. When embedded into steel-reinforced mortar beams, their results reported steep increases in the electrical resistance of the sensors indicating the appearance of flexural cracks in the host structure. More recently, Downey et al. [10] proposed a novel piezoresistive clay brick for crack detection applications in masonry structures. On the basis of an experiment on a small-scale masonry wall equipped with three inserted smart bricks, the variations of the electrical output in the sensing bricks were reported effective to detect variations in the compression loading paths and the appearance of cracks. Finally, the deployment of smart piezoresistive films offers an intermediate solution. Such systems work as a conductive sensing skin when a crack appears in the contact with the underlying structure, what results in a dislocation of the sensing strips and, therefore, in a change in the electrical resistance of the sensor. Nonetheless, in virtue of the piezoresistive properties of such composites, it is also possible to relate the monitored strain state to the presence of damages far from the sensing strips. In this line, it is worth noting the works by Kang *et al.* [22] who developed 10wt.% MWCNT-reinforced Poly(methyl methacrylate) (PMMA) strain sensors. Under laboratory conditions, the authors bonded MWCNT/PMMA sensors with dimensions 50x4x0.08 mm^3 to an aluminum cantilever using a spray-on technique. Their results demonstrated the ability of the sensing strips for damage localization of prescribed damages.

While important advances have been done from experimentation, the number of theoretical works that allows for optimizing and tailoring self-sensing MWCNT-based sensors is much scarcer. In particular, the modeling of the behavior of MWCNT-based composites for SHM applications must cope with both their mechanical and electrical properties. Firstly, motivated by the reported remarkable stiffness, high aspect ratio, and low mass density of MWCNTs [23, 24], considerable efforts have been devoted to the mechanical homogenization of MWCNT-based composites. The stiffening efficiency of MWCNTs is attributed to the load transfer mechanisms from matrix to

fillers through weakly non-bonded van der Waals (vdW) forces at the nano-scale. Therefore, the homogenization process is, in essence, a bottom-up multi-scale problem where the atomic information must be scaled up to the macro-scale. The most common approaches in the literature include [25]: continuum modeling, Molecular Dynamics (MD) simulations, atomistic-based continuum modeling, and mean-field homogenization with interfacial effects. The method of MD simulations permits the study of the atomic structure of MWCNTs and their interaction with the matrix material. However, the application of MD simulations to realistic systems with a representative number of atoms usually entails unaffordable computational demands. Secondly, continuum mechanics-based models assume that MWCNTs can be modeled as continuum structures, namely beams, shells or solids. Nevertheless, the correctness of such assumptions is questionable because the fundamentals of classical continuum mechanics are no longer valid at the nanoscale. Atomistic-based continuum techniques assume certain relations between the interatomic potentials and the stiffness of continuum structures such as truss rods or link elements. In this way, it is possible to describe the atomistic structure of the composite through a continuum framework such as Finite Element (FE) modeling with moderate computational costs [26]. Finally, mean-field homogenization approaches with interfacial effects offer a simplified alternative by considering the load transfer mechanisms as certain mechanical conditions at matrix/MWCNT interfaces. In this line, different approaches can be found in the literature including spring-type interface models [27], functionally graded interface models [28], and interphase or core-shell models [29]. In the latter, the load transfer mechanisms are taken into account through coating phases with finite volumes surrounding the inclusions.

With regard to the electrical properties of MWCNT-based composites, the number of theoretical studies is even lower and it remains an open issue in the literature. The electrical conductivity of MWCNT-based composites has been extensively reported in the literature to be percolative-type [30, 31]. Such behavior is characterized by a sharp increase in the overall conductivity when the filler concentration reaches a critical value, termed "percolation threshold". Below percolation, the transfer of electrons is only possible by an electron hopping mechanism, that is, a quantum tunneling effect. For increasing concentrations, only small increases are observed in the overall conductivity until fillers can touch each other resulting in a continuous electrically conductive path. The percolation threshold denotes the onset of such process, also known as conductive networking mechanism. On this basis, the self-sensing capabilities of these composites are ascribed to strain-induced alterations of these conductive mechanisms. In particular, three primary strain-induced alterations have been reported [32, 33]: (i) variations of the effective filler volume fraction, (ii) filler reorientation, and (iii) changes in the inter-particle properties. Along these lines, it is worth noting the works of Deng and Zheng [34] and Takeda *et al.* [35] who incorporated the percolative-type behavior of MWCNT/polymer composites into a simplified micromechanics model of the overall electrical conductivity. Feng and Jiang [36] devised a mixed Mori-Tanaka micromechanics model to account for the separate influence of electron hopping and conductive networking mechanisms on the electrical conductivity of MWCNT/polymer composites. In that work, the electron hopping mechanism was simulated by means of conductive interphases surrounding the MWCNTs, while the conductive networks were accounted for by changes in the fillers aspect ratios. With regard to the modeling of the strain sensitivity of MWCNT-reinforced composites, the number of works is considerably scarce. A noteworthy contribution was done by Alamusi and Hu [37] who utilized a three-dimensional resistor network, including Simmon's contact resistance between MWCNTs and fillers re-orientation. Tallman and Wang [38] extended the theoretical formulation developed by Takeda *et al.* [35] for the piezoresistivity modeling of MWCNT-based composites under arbitrary dilations. It is also worth noting the works of Feng and Jiang on the modeling of uni-axial [32] and bi-axial [39] strain sensitivity of MWCNT/polymer composites. Those authors proposed considering the strain-induced reorientation of the fillers through statistical Orientation Distribution Functions (ODFs). Recently, the authors extended a mixed Mori-Tanaka micromechanics approach for the modeling of the uni-axial strain sensitivity of MWCNT-reinforced cement-based composites [33] to arbitrary three-dimensional strain states [40].

In light of the literature review, this paper presents a theoretical study aimed at investigating the potential application of MWCNT-based sensing strips for damage detection/localization/quantification in RC beam-like structures. In particular, a multisectioned MWCNT/epoxy strip-like sensor is proposed to be deployed for monitoring the strain distribution along beam structures. Epoxy is chosen as matrix material due to its relatively low unit cost and easy processing, allowing designing sensors with a variety of geometries adaptable to pre-existing structures. The study of smart MWCNT-reinforced large-scale sensors implies two major levels, namely the constitutive characterization of the material and the macroscopic electromechanical response of the sensor. To the best understanding of the authors, there is no generalized theoretical framework apt to tackle such problem. In order to fill this lacuna, this work presents the application of a micromechanics-based FE model for the electromechanical analysis of MWCNT/epoxy strip-like sensors. Furthermore, a damage detection algorithm through model updating approach is presented. To do so, an Euler-Bernoulli model for beams equipped with a smart MWCNT/epoxy strip is developed. Finally, two case studies are presented including: a 2D concrete beam with multiple prescribed crack-like damages, and a 3D RC beam under four-point flexural conditions with non-prescribed smeared cracks.

The remainder of this paper is organized as follows: Section 2 presents the proposed multisectioned smart MWCNT/epoxy strips and details the employed measurement setup. Moreover, the constitutive modeling of MWCNT-based composites is concisely overviewed. Section 3 introduces a damage identification algorithm through model updating of an Euler-Bernolli beam model of beams equipped with MWCNT/epoxy strip-type sensors. Section 4 presents the numerical results and related discussion and, finally, Section 5 concludes the work.

2. Multisectioned smart MWCNT/epoxy strip-type strain sensor

2.1. Geometry description and measurement setup

The smart beams analyzed in this research work are sketched in Fig. 1(a). As an example, we are considering a simply supported precast RC beam of length L, width B and depth h with a MWCNT/epoxy strip-like strain sensor of thickness h_c deployed on the upper part of the beam. The proposed smart beams are aimed at detecting, localizing and quantifying damages by exploiting local changes in electrical resistivity of the sensing strip. For this purpose, the sensing strip is multi-sectioned by $n+1$ equally spaced electrodes. Inspired by the work of Downey et al. [19] on reinforced self-sensing concrete structures, the measurement setup proposed in this work is shown in Fig. 1(b). The measurement scheme consists of n in-series resistors representing the sections of the sensing strip, an in-line shunt resistor R_{shunt} linked between the power source and the first electrode, and the last $n+1$-th electrode connected to ground. The resistance between electrodes k and $k+1$, R_k, is calculated by dividing the measured voltage difference, V_k, by the current intensity, I, flowing through the strip's cross-section as:

$$R_k = \frac{V_k}{I} \tag{1}$$

and the current I is obtained by monitoring the voltage drop, V_o, across the in-line shunt resistor, R_{shunt}, that is:
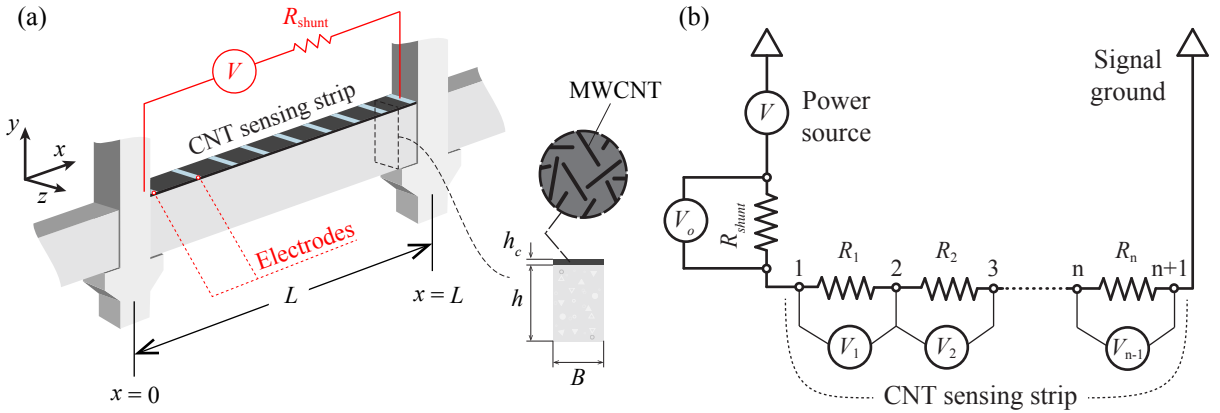
$$I = \frac{V_o}{R_{shunt}} \tag{2}$$

Figure 1: (a) Schematic representation of MWCNT/epoxy strip-like strain sensor on a simply supported precast RC beam, and (b) electrical resistivity measurement setup.

Self-sensing composite materials doped with carbon nano-inclusions are known to exhibit an inherent time-based drift in their electrical output when connected to Direct Current (DC) power sources [41]. This drift usually manifests as an increase in the resistance in time, often termed polarization. As a solution, it has been reported in the literature that the use of Alternating Current (AC) power sources minimizes the effect of this drift [42]. Nonetheless, conventional LCR meters (inductance, capacitance and resistance) are not typically applicable to multichannel measurements, which are essential for damage detection and localization. An effective alternative is the biphasic DC measurement technique proposed by Downey et al. [43] for resistivity measurements in MWCNT-doped self-sensing concrete structures. This technique consists of applying periodic measure/discharge square waves and conducting DC resistivity measurements during the measurement regions of the waves. Those authors demonstrated that such measurement approach provides stable multi-channel resistance readings through continuously charging and discharging the composite. Therefore, theoretical simulations limited to the steady-state response of the system are in line with available technical possibilities.

2.2. Micromechanics-based FE electromechanical modeling of smart MWCNT/epoxy sensing strips

In this section, the electromechanical constitutive properties of MWCNT/epoxy sensing strips are computed by a mixed micromechanics approach. Then, the macroscopic response of the sensing strips are modeled by means of a micromechanics-based FE approach. For notational convenience, blackboard bold letters are used to denote fourth-order tensors, while bold letters indicate second-order tensors.

2.2.1. Elastic properties of MWCNT/epoxy sensing strips

Firstly, the elastic moduli of MWCNT-reinforced epoxy are computed by a micromechanics approach. In order to take into account the interfacial properties, an interphase or core-shell model is used [29, 44]. Along these lines, the interface regions are simplified to coating phases with constant thickness t surrounding the fillers. Then, the composite is defined as a three-phase composite consisting of a hosting matrix, inclusions and surrounding interphases with fourth-order elastic tensors $\mathbb{C}_m$, $\mathbb{C}_p$ and $\mathbb{C}_i$, respectively. Subscripts "p", "i", and "m" refer the corresponding quantity to the filler, interphase and matrix, respectively. Considering a Representative Volume Element (RVE) of a linear elastic matrix doped with a statistically representative population of MWCNTs, the overall constitutive tensor of the three-phase composite reads [45]:

$$\overline{\mathbb{C}} = \left(f_m \mathbb{C}_m + f_i \langle \mathbb{C}_i : \mathbb{A}_i \rangle + f_p \left\langle \mathbb{C}_p : \mathbb{A}_p \right\rangle \right) : \left(f_m \mathbb{I} + f_i \langle \mathbb{A}_i \rangle + f_p \left\langle \mathbb{A}_p \right\rangle \right)^{-1} \tag{3}$$

where angle brackets $\langle \cdot \rangle$ represent orientational average, and a colon between two tensors denotes inner product, $\mathbb{A} : \mathbb{B} \equiv A_{ijkl} B_{klmn}$. The terms f_p, f_i, and f_m stand for the volume fraction occupied by the fillers, the interphases and the matrix, respectively. The expression of the volume fraction of the interphases f_i can be found in Xu *et al.* [46]. The terms $\mathbb{A}_i$ and $\mathbb{A}_p$ denote the concentration factors for interphases and inclusions, respectively, and can be written in terms of the corresponding dilute concentration tensors, $\mathbb{A}_i^{dil}$ and $\mathbb{A}_p^{dil}$, as:

$$\mathbb{A}_\chi = \mathbb{A}_\chi^{dil} : \left(f_m \mathbb{I} + f_i \mathbb{A}_i^{dil} + f_p \mathbb{A}_p^{dil} \right)^{-1}, \quad \chi = p, i \tag{4}$$

$$\mathbb{A}_\chi^{dil} = \mathbb{I} + \mathbb{S} : \mathbb{T}_\chi, \quad \chi = p, i \tag{5}$$

with

$$\mathbb{T}_\chi = -\left(\mathbb{S} + \mathbb{M}_\chi \right)^{-1}, \quad \chi = p, i \tag{6}$$

$$\mathbb{M}_\chi = \left(\mathbb{C}_\chi - \mathbb{C}_m \right)^{-1} : \mathbb{C}_m, \quad \chi = p, i \tag{7}$$

2.2.2. Electrical properties of MWCNT/epoxy sensing strips

Numerous experimental and theoretical studies agree to point out that the electrical conductivity of MWCNT-reinforced polymer composites exhibit a percolative-type behavior [30, 31]. On this basis, when $f_p < f_c$, f_c being the percolation threshold, fillers are very distant and the transfer of electrons is only possible through the electron hopping mechanism. Once the MWCNT volume fraction reaches the percolation threshold ($f_p \geq f_c$), some fillers begin forming conductive networks and both mechanisms, namely electron hopping and conductive networking mechanisms, act simultaneously as schematically represented in Fig. 2 (a).
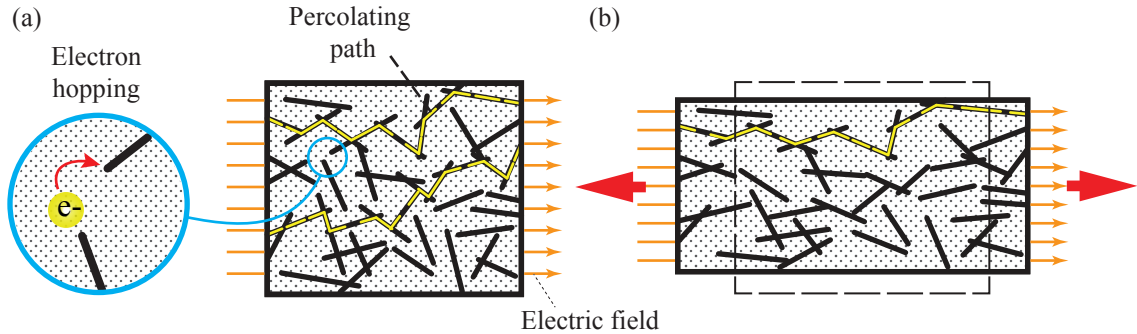

Figure 2: Schematic representation of the contribution of electron hopping and conductive network mechanisms to the overall electrical conductivity of MWCNT nanocomposites (a), and strain-induced filler reorientation and volume expansion (b).

The electron hopping mechanism can be modeled as a conductive interphase surrounding the nanotubes, whilst the conductive networking mechanism can be simulated by variations of the filler aspect ratio [36]. In the first

case, the electrical resistivity of the interphases is typically computed by the generalized Simmons' formula as follows [47]:

$$R_{int}(d_a) = \frac{d_a \hbar^2}{ae^2 (2m\lambda^{1/2})} \exp\left(\frac{4\pi d_a}{\hbar} (2m\lambda)^{1/2}\right) \tag{8}$$

where m and e are the mass and the electric charge of an electron, respectively, λ is the height of the tunneling potential barrier, a is the contact area of the MWCNTs, and $\hbar$ stands for the reduced Planck's constant. The term d_a stands for the average distance between MWCNTs without electrical contacts, and is a function of the cut-off distance for tunneling effects d_c [36]. The equivalent conductivity of the MWCNT/interphase assemblage is defined as transversely isotropic and its expression can be found in references [36, 48].

The micromechanics framework is defined considering a RVE of a polymer matrix with electrical conductivity σ_m doped with a sufficient number of fillers with conductivity σ_c. Hence, the Mori-Tanaka estimation of the overall electrical conductivity tensor of the nanocomposite can be defined in a piecewise form as follows [49]:

$$\boldsymbol{\sigma}_{eff} = \boldsymbol{\sigma}_m + (1 - \xi) \langle \Gamma_{EH} \rangle + \xi \langle \Gamma_{CN} \rangle \tag{9}$$

with:

$$\Gamma_{EH} = f_{eff} (\boldsymbol{\sigma}_{EH} - \boldsymbol{\sigma}_m) \boldsymbol{A}_{EH} \tag{10a}$$

$$\Gamma_{CN} = f_{eff} (\boldsymbol{\sigma}_{CN} - \boldsymbol{\sigma}_m) \boldsymbol{A}_{CN} \tag{10b}$$

and ξ the fraction of percolated MWCNTs [34]:

$$\xi = \begin{cases} 0, & 0 \le f_p < f_c \\ \dfrac{f_p^{1/3} - f_c^{1/3}}{1 - f_c^{1/3}}, & f_c \le f_p \le 1 \end{cases} \tag{11}$$

The term A in Eq. (10) denotes the electric field concentration tensor, and σ_m and σ_c stand for the second-order electrical conductivity tensors of the matrix and the interphase/filler assemblage [36], respectively. Subscripts EH and CN refer to electron hopping and conductive networking mechanisms, respectively. In the case of MWCNTs forming conductive networks, several nanotubes are electrically connected and, therefore, can be assumed as infinitely-long fillers [50].

According to the formulation outlined above, the strain-sensing capabilities are ascribed to strain-induced tampering of the electron hopping and conductive networking mechanisms [32, 51] as schematically represented in Fig. 2 (b). In particular, three major changes are expected when MWCNT-reinforced composites are subjected to an external mechanical deformation [32, 33, 38]:

(i) Volume expansion and reorientation of MWCNTs:

Two different strain states are considered, namely dilation and distortion. When composites are subjected to dilation strains, and assuming that the fillers remain inextensible because of their considerably higher stiffness compared to that of the matrix, the volume expansion induces changes in the MWCNT volume fraction as follows [40]:

$$f_p = \frac{f_p^o}{\bar{\varepsilon}_1 \bar{\varepsilon}_2 \bar{\varepsilon}_3} \tag{12}$$

where f_p^o stands for the filler volume fraction of the unstrained system, and $\bar{\varepsilon}_i = \varepsilon_i + 1$, $i=1,2,3$, with ε_i denoting the strain in the global coordinate axis x_i, $i=1,2,3$. Likewise, dilation strains also originate a re-alignment of fillers, which can be determined by means of a statistical ODF, $p(\psi',\beta')$ as follows [40]:

$$p(\psi',\beta') = \frac{\bar{\varepsilon}_1^2 \bar{\varepsilon}_2^2 \bar{\varepsilon}_3^2}{\left[\bar{\varepsilon}_2^2 \bar{\varepsilon}_1^2 \cos^2 \beta' + \bar{\varepsilon}_3^2 \left(\bar{\varepsilon}_2^2 \cos^2 \psi' + \bar{\varepsilon}_1^2 \sin^2 \psi'\right) \sin^2 \beta'\right]^{3/2}} \tag{13}$$

with $\psi \in [0, 2\pi]$ and $\beta \in [0, \pi/2]$ being the Euler angles. A comma indicates an Euler angle in the deformed configuration.

Conversely, the application of distortion strains does not originate any volume change. Nonetheless, distortions do induce re-orientation of fillers which, in the particular case of ε_{32}, can be described by an ODF as [40]:

$$p(\psi,\beta') = \left(1 - 4\varepsilon_{32} \sin \psi \sin \beta' \cos \beta' + 4\varepsilon_{32}^2 \sin^2 \psi \sin^2 \beta'^2\right)^{-3/2} \tag{14}$$

6

(ii) Change in the conductive networks:

The re-orientation of fillers decreases the randomness of the MWCNT distribution and, consequently, also reduces the likelihood of forming conductive paths. In other words, the re-orientation of fillers leads to increases in the percolation threshold f_c. Assuming MWCNTs as rod-like inclusions, the strain-induced variation of the percolation threshold can be directly related to the ODFs from Eqs. (13) and (14) through the Komori and Makishima's approach [52] as shown in reference [33].

(iii) Change in the tunneling resistance:

Finally, the action of external strains also alters the fillers' separation and, consequently, the electron hopping mechanism [53]. Hence, some research studies assume that, at relatively low strains, the inter-particle distance and the height of the potential barrier change proportionally to the strain as follows [54]:

$$
\begin{aligned}
d_a &= d_{a,0}(1 + C_1 \varepsilon_i), \\
\lambda &= \lambda_0(1 + C_2 \varepsilon_i)
\end{aligned}
\tag{15}
$$

where $d_{a,0}$ and λ_0 are the initial inter-particle distance and potential height of the unstrained system. Due to the lack of information in the literature about explicit expressions for these quantities, the proportionality constants C_1 and C_2 are usually obtained by fitting experimental data.

2.2.3. Electromechanical modeling of piezoresistive MWCNT-reinforced structures

Modeling the piezoresistive behavior of MWCNT-reinforced smart composites under arbitrary 3D strain states requires linking the constitutive equations governing the electrical behavior of the material with those describing the mechanical strain state or, alternatively, the stress state assuming a linearly elastic material. On the basis of the previously presented micromechanics approach, the electrical resistivity tensor ρ_{eff}, which can be directly computed as the inverse of the conductivity tensor σ_{eff} in Eq. (9), i.e. $\rho_{eff} = \sigma_{eff}^{-1}$, can be related to the strain in the composite through:

$$
\rho_{eff} = \rho_{eff}^o (I + r)
\tag{16}
$$

where $\rho_{eff}^o = (\sigma_{eff}^o)^{-1}$ is the resistivity tensor of the unloaded composite and r is the relative change in resistivity defined as $r = \Pi \varepsilon$. The connection between the relative change in resistivity and the strain tensor is the Π matrix, whose components are denoted as λ_{ij}. It is hypothesized that MWCNT-reinforced composites possess cubic crystal symmetry, similarly to silicon [55], and thus only three $\lambda-$coefficients are needed to fully characterize the matrix Π. Hence, the expression $r = \Pi \varepsilon$ becomes in matrix notation:

$$
\begin{Bmatrix} \Delta\rho_1/\rho_0 \\ \Delta\rho_2/\rho_0 \\ \Delta\rho_3/\rho_0 \\ \Delta\rho_4/\rho_0 \\ \Delta\rho_5/\rho_0 \\ \Delta\rho_6/\rho_0 \end{Bmatrix} = \begin{bmatrix} \lambda_{11} & \lambda_{12} & \lambda_{12} & 0 & 0 & 0 \\ \lambda_{12} & \lambda_{11} & \lambda_{12} & 0 & 0 & 0 \\ \lambda_{12} & \lambda_{12} & \lambda_{11} & 0 & 0 & 0 \\ 0 & 0 & 0 & \lambda_{44} & 0 & 0 \\ 0 & 0 & 0 & 0 & \lambda_{44} & 0 \\ 0 & 0 & 0 & 0 & 0 & \lambda_{44} \end{bmatrix} \begin{Bmatrix} \varepsilon_{11} \\ \varepsilon_{22} \\ \varepsilon_{33} \\ 2\varepsilon_{23} \\ 2\varepsilon_{13} \\ 2\varepsilon_{12} \end{Bmatrix}
\tag{17}
$$

The term λ_{11} depicts the piezoresistive effect along one principal crystal axis for strains applied in this principal crystal axis (longitudinal piezoresistive effect), λ_{12} relates the piezoresistive effect along one principal crystal axis for strains applied in one perpendicular crystal axis (transverse piezoresistive effect), and λ_{44} describes the piezoresistive effect on an out-of-plane electric field by the change of the in-plane current induced by in-plane shear stress. In order to compute the independent coefficients in Π, only two virtual experiments are needed as indicated in reference [40], namely laterally constrained uni-axial dilation and distortion. To do so, the relative variation of the electrical resistivity terms, $\Delta\rho_i/\rho_0$ with i=1,...,6, can be obtained according to the micromechanics approach previously presented in Section 2.2.3. Firstly, assuming laterally constrained uni-axial dilations (ε_{ij}=0 expect for ε_{11}, ε_{22} or ε_{33}), the piezoresistivity coefficients λ_{11} and λ_{12} can be obtained from Eq. (17). Secondly, λ_{44} can be computed considering pure distortion strain states (ε_{ij}=0 except for ε_{23}, ε_{13} or ε_{12}). Finally, the computed constitutive electromechanical properties can be used in a FE multiphysics code to simulate the macroscopic response of three-dimensional MWCNT-based composites.

3. Damage detection algorithm based on MWCNT/epoxy strip-like strain sensors deployed on beam-like structures

In this section, a damage detection, localization and quantification algorithm is proposed through modal updating of a fast and cost-efficient piezoresistive Euler-Bernoulli beam model of smart beams under static loadings.

3.1. Euler-Bernoulli beam model of elastic smart beams under static loadings

An Euler-Bernoulli beam model is developed for the static analysis of elastic beams equipped with a smart MWCNT/epoxy strip-like strain sensor as sketched in Fig. 3. The system consists of a smart strip with thickness h_c attached onto a host beam with a length of L and a rectangular cross section of width B and depth h. Following the hypothesis of rigid in-plane deformation of cross sections in the Euler-Bernouilli beam theory, it is assumed that the thickness of the strip remains constant during deformations. Therefore, the variation of the electrical resistivity is only sustained by the longitudinal piezoresistivity coefficient λ_{11}. Additionally, in order to incorporate the presence of damages, the beam is divided into n elements with constant piecewise bending stiffness EI_k with k=1,...,n. Hence, an elemental non-dimensional damage parameter D_k can be defined in terms of the ratio between the damaged element stiffness and the undamaged value EI_r (reference model), i.e. $D_k = 1 - EI_k/EI_r$. It is also assumed that $n+1$ electrodes, labeled as E_j with j=1,...,n+1, are located in the sensing strip at both extremes of every beam element. In this way, and following the measurement setup previously presented in Fig. 1 (b), a shunt resistor R_{shunt} is connected in series between the voltage source and the first electrode E_1, while the last electrode E_{n+1} is connected to ground. Overall, the sensing system behaves like a series circuit with n resistors R_k representing the local internal resistances of the sensing strip. Hence, the bending strain in every section of the beam can be inferred through the voltage drop at every section $V_k = R_k I$, with I being the electrical current flowing in the system.
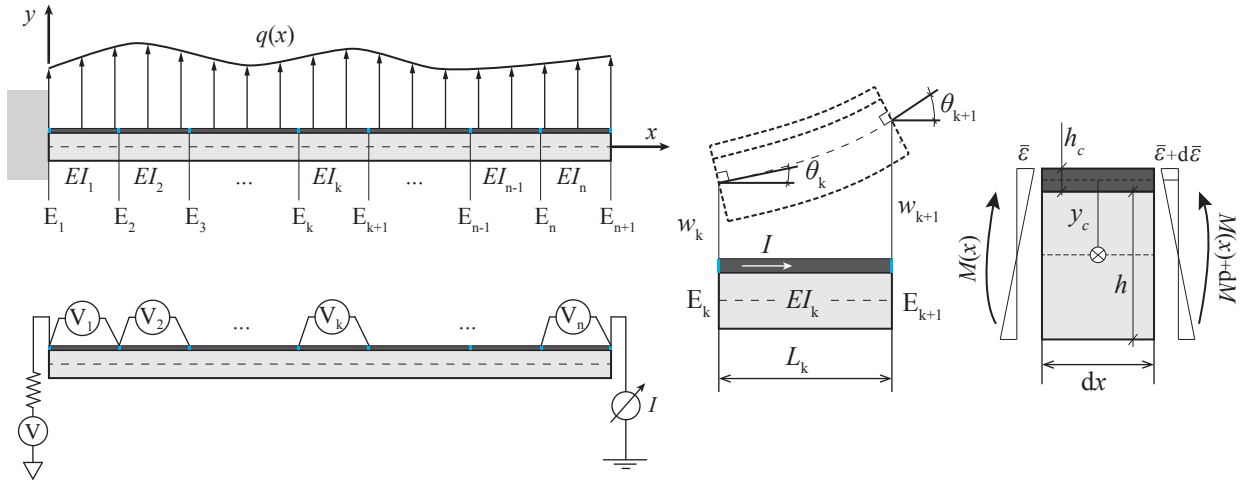

Figure 3: Schematic of an Euler-Bernoulli beam with a smart MWCNT/epoxy strip-like strain sensor.

Let us focus on one element k with length L_k. Assuming uni-axial piezoresistivity, the electrical resistivity under a general transverse loading $q(x)$ can be readily computed as $\rho(x) = \rho_o(1+\lambda_{11}\bar{\varepsilon})$, with ρ_o being the unstrained resistivity and $\bar{\varepsilon}$ the axial strain in the sensing strip. In order to capture the variation of the axial strain across the element, let us define an infinitesimal segment of beam of length dx. Considering the Bernoulli-Navier assumption of linear distribution of axial strain across the section height, the electrical resistance of the infinitesimal segment can be computed by the second Ohm's law as follows:

$$dR_k(x) = \frac{\rho(x)dx}{h_c B} = \frac{\rho_o \left(1 - \lambda_{11}M(x)y_c/EI_k\right) dx}{h_c B}, \quad x \in (x_k, x_{k+1}) \tag{18}$$

where $M(x)$ is the bending moment at x and y_c is the depth of the neutral axis from the centerline of the strip. Therefore, the total electrical resistance of the beam element k can be calculated by integrating Eq. (18) as:

$$R_k = \int_{x_k}^{x_{k+1}} dR_k(x) = \frac{\rho_o}{h_c A}\left(L_k - \lambda_{11}y_c \int_{x_k}^{x_{k+1}} \frac{M(x)}{EI_k}dx\right) = \frac{\rho_o}{h_c A}\left(L_k - \lambda_{11}y_c(\theta_{k+1} - \theta_k)\right) \tag{19}$$

with θ_{k+1} and θ_k being the rotations of the beam's axis at its extremes k+1 and k, respectively. It is noted from Eq. (19) that the sensing strip essentially behaves as a curvature sensor. Finally, the previous definition in Eq. (18) can be extended to a general continuous beam with bending stiffness $EI(x)$ as follows:

$$R'(x) = \frac{\rho_o}{h_c A}\left(1 - \lambda_{11}\frac{M(x)y_c}{EI(x)}\right) \approx \frac{\rho_o}{h_c A}\left(1 - \lambda_{11}y_c w''(x)\right) \tag{20}$$

8

where $w(x)$ stands for the vertical deflection of the beam axis at x and a prime indicates derivative with respect to x. The expression in Eq. (20) synthesizes the fundamental sensing principle of the proposed smart beams. Thence, the variation of the electrical resistance between two points of the sensing strip depends linearly upon the curvature ($\approx w''(x)$), the electrical resistivity of the composite (ρ_o), the longitudinal piezoresistivity coefficient (λ_{11}), and the distance of the sensor from the neutral axis of the beam (y_c), whilst it is inversely proportional to the cross-sectional area of the strip ($h_c A$). Hence, the electrical resistance between the power source and an arbitrary point at a distance x can be readily obtained by integrating Eq. (20) what leads to:

$$R(x) = \frac{\rho_o}{h_c A} \left[x - \lambda_{11} y_c \left(w'(x) - \theta_o \right) \right] + R_{shunt} \tag{21}$$

Note that the boundary condition on the electrical resistance at $x = 0$ is $R(0)=R_{shunt}$. Finally, the total electrical resistance between the extremes of the sensor can be obtained by evaluating the previous equation at $x=L$:

$$R_{tot} = R(L) = \frac{\rho_o}{h_c A} \left[L - \lambda_{11} y_c \left(\theta_{n+1} - \theta_o \right) \right] + R_{shunt} \tag{22}$$

and the electrical current in the system I can be obtained by Ohm's law as follows:

$$I = V/R_{tot} \tag{23}$$

Interestingly, it is noted from Eqs. (22) and (23) that the electrical current is insensitive to the piezoresistive properties of the sensor when the rotations of the beam are equal at the extremes. The proposed beam model has been implemented in a FE code with two-noded Hermite-cubic EulerBernoulli beam elements, including two degrees of freedom per node (w,θ).

3.2. Damage identification through beam model updating

The goal of this section is to propose an algorithm able to identify the presence and severity of damages in the beam through the electrical outputs of the smart strip. To this aim, the previously introduced Euler-Bernoulli model for the smart beam can be used for damage detection/localization/quantification through model updating. Model updating is a branch of optimization wherein the differences between a model's estimates and their experimental counterparts are minimized using mathematical techniques. In particular, a vector containing the electrical resistances of the n beam sections between every two electrodes, $\overline{R} \in \mathbb{R}^n$, is defined as the function values. The residual vector is defined as the difference between the outputs calculated by the beam model and those obtained from experimentation, $\overline{R}_{dam}$. Here, the appearance of finite residuals is ascribed to the presence of structural damages locally affecting the bending stiffness constants of the beam, which are defined as the design variables. In this framework, the proposed damage detection/localization/quantification algorithm is summarized in the flowchart depicted in Fig. 4. In order to define a denser stiffness map, the beam sections are divided into n_d sub-elements and, therefore, the components of the design vector $\overline{EI}$ can be written as EI_j with j=1, $n_d \cdot$n. In this way, the beam model is updated in order to reproduce the experimental measurements and thereby obtain the position and severity of damages. It is important to note that the present approach requires to know beforehand the loading and boundary conditions.
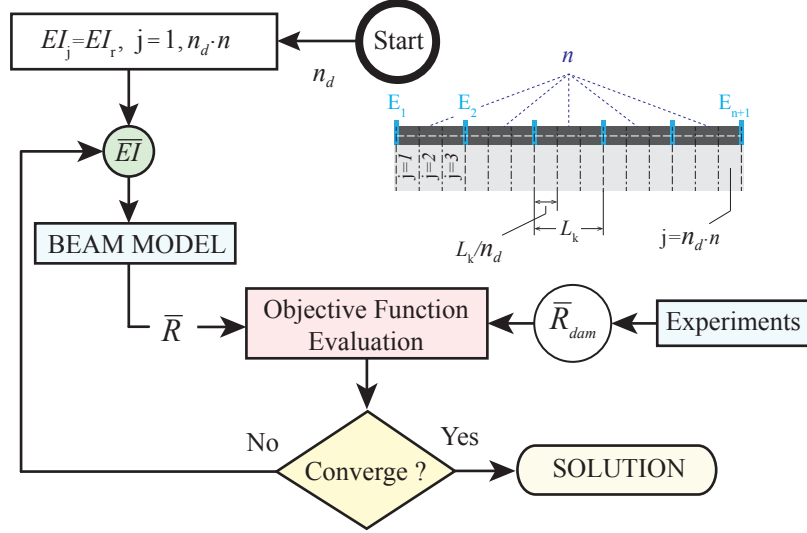
Figure 4: Flowchart of damage identification through model updating.

Ill conditioning limitations of model updating in the field of SHM have been extensively reported in the literature [56]. In the case of an ill-conditioned system, the design variables in different sets can produce the same set of responses at distinct locations of the search space and, hence, the solution cannot be affirmed as unique. In this work, a simple regularization technique is incorporated as a weighted norm of the parameter changes to keep the parameter variations small. In other words, the physical assumption of the implemented regularization imposes that the design variables remain close to those of the undamaged system. Therefore, the minimization problem is defined as follows:

$$\overline{EI} = \arg \min_{\overline{EI} \in \mathbb{D}} \left(\left\| \overline{R} - \overline{R}_{dam} \right\| + \beta \left\| \overline{EI} - \overline{EI}_r \right\| \right) \tag{24}$$

with the design space $\mathbb{D}$ defined as:

$$\mathbb{D} = \left\{ \overline{EI} \in \mathbb{R}^{n_d \cdot n} : 0 \le EI_j \le EI_r \right\} \tag{25}$$

where β is a tradeoff parameter between the two parts of the cost function. For small values of β, the design variables are almost unrestricted and the solution resembles the original ill-posed problem. Conversely, for large values of β, the design variables are highly constricted and large errors may arise in the solution. In this regard, various techniques to compute convenient values of the tradeoff parameter can be found in the literature (see e.g. [57]). In this work, a simple sensitivity analysis showed that a value of β=0.001 provides reasonably good solutions for the purpose of this research.

4. Numerical results and discussion

The aim of this section is twofold. Firstly, to illustrate the application of the presented micromechanics-based FE modeling of the electromechanical response of MWCNT/epoxy strip-like strain sensors. Secondly, to demonstrate the capabilities of the proposed resistivity measurement scheme and model updating algorithm for damage detection, localization and quantification. In particular, two theoretical case studies are presented, namely 2D smart beams with multiple prescribed crack-like damages, and 3D smart beams with non-prescribed cracking under four-point flexural conditions through a smeared crack model. Accordingly, this section has been divided into three subsections as follows: Subsection 4.1 presents the effective electromechanical properties of MWCNT/epoxy composites on the basis of experimental benchmark results retrieved from the literature; and Subsections 4.1 and 4.2 present the two considered case studies.

4.1. Effective electromechanical properties of MWCNT/epoxy composites

Firstly, the electromechanical properties of MWCNT/epoxy sensing strips are computed on the basis of the micromechanics approach previously overviewed in Section 2. To this aim, the experimental results from references [9], [8] and [24] are used as validation basis for the piezoresistivity coefficients, electrical conductivity and mechanical properties of MWCNT/epoxy composites, respectively. Firstly, the electrical properties of

MWCNT/epoxy composites are computed considering eight micromechanical variables in a nonlinear regression model, including the length of the MWCNTs ($L \in [0.1 - 30]$ μm [24, 32, 48]), the diameter of the MWCNTs ($D \in [10 - 20]$ nm [24, 32]), the electrical conductivity of the MWCNTs ($\sigma_c \in \left[10^1 - 10^4\right]$ S/m [36]), the mass density of the MWCNTs ($m^{cnt} \in [1.4 - 2.25]$ g/cm^3 [58]), the height of the potential barrier ($\lambda \in [0.5 - 2.5]$ eV [9]), and the proportionality constants C_1 and C_2 ($C_1 \in [0 - 20]$, $C_2 \in [0 - 2]$). The Poisson's ratio, the mass density and the electrical conductivity of the epoxy matrix are selected as constant values, ν_m=0.28, m^m=1.12 g/cm^3 [59] and σ_m=1.04E-10 S/m [8]. Secondly, the elastic modulus of the interphases E_i and the interphase thickness t are also computed by a nonlinear regression model on the basis of the experimental results reported by Vahedi *et al.* [24]. The Young's modulus and Poisson's ratio of the epoxy matrix are selected as E_m=2.5 GPa and ν_m=0.28, respectively. With regard to the elastic modulus of MWCNTs, E_{cnt}, experimental results in the literature report variations from 270 to 959 GPa [60]. For simplicity, a Young's modulus of 700 GPa is selected and MWCNTs are considered as isotropic solid rod-like inclusions. As a result, the fitted micromechanical variables are collected in Table 1 and the comparison results with experimental data are provided in Table 2. Note that, as in common practice, the filler content is expressed in terms of the mass fraction of MWCNTs w_p, which is related to the filler volume fraction, f_p, as:

$$f_p = \frac{w_p}{w_p + (m^{cnt}/m^m) - (m^{cnt}/m^m)w_p} \tag{26}$$

with m^{cnt} and m^m being the mass densities of the filler and matrix phases, respectively.

It can be observed in Table 2 that the present approach provides estimates of the Young's moduli of the composites in very close agreements with the experimental data, reaching maximum differences below 5%. With regard to the electrical properties, note that the piezoresistivity coefficients are labeled with the superscript "+" to indicate that such values were determined by Sanli et al. [9] through uni-axial direct tensile tests. Following the procedure presented in reference [33], the piezoresistivity coefficients are calculated as the slope of a linear regression of the curves of relative variation of resistivity versus applied strain ($\Delta\rho/\rho_o$ vs. ε). It is noted in Table 2 that, although relatively larger discrepancies are found between the theoretical and the experimental results, the estimates of the micromechanics approach show very similar tendencies for both the piezoresistivity coefficients λ_{11}^+ and the effective conductivities σ_{eff}. The percolation threshold is around f_c=0.3 wt.% as reported by Sanli et al. [9] and accurately captured by the present approach. It is observed that the strain-sensitivity is maximum for filler contents close to the percolation threshold, while higher filler contents lead to less sensitive composites. Moreover, the electrical conductivity is governed by a percolative-type behavior and, accordingly, limited increases are found in the overall conductivity for filler contents above the percolation threshold. It is important to remark that all the fitted micromechanical variables in Table 1 have been assumed as constant within the whole range of filler contents for consistency purposes. Nevertheless, micromechanical parameters such as the inter-particle distance d_a, the height of the potential barrier λ, or the proportionality constants C_1 and C_2, are presumably functions of the filler volume fraction. Hence, and in view of the large uncertainty in the definition of the micromechanical variables and repeatability of MWCNT-based composites, the present approach is considered suitable for the purpose of the present work.

Table 1: Fitted micromechanical variables of MWCNT/epoxy composites.

L_{cnt}	3.21 μm	E_{cnt}	700 GPa
D_{cnt}	10.35 nm	E_m	2.5 GPa
d_c	0.22 nm	ν_m	0.28
λ	0.69 eV	ν_{cnt}	0.3
σ_c	1.00E+02 S/m	t	31.00 nm
σ_m	1.04E-10 S/m	E_i	2.17 GPa
C_1	12.47	m^{cnt}	1.42 g/cm^3
C_2	1.02	m^m	1.12 g/cm^3

Table 2: Comparison of experimental and micromechanics estimates of the electromechanical properties of MWCNT/epoxy composites.

	Ref.	0.30 wt.%	0.40 wt.%	0.50 wt.%	0.75 wt.%	1.00 wt.%
λ_{11}^+	[9]	15.39	8.37	3.85	3.04	2.86
λ_{11}^+	Present	15.41	7.05	5.49	3.39	2.13
σ [S/m]	[8]	1.50E-03	4.80E-03	9.60E-03	4.32E-02	1.01E-01
σ [S/m]	Present	1.50E-03	5.50E-03	1.22E-02	3.53E-02	6.56E-02
	Ref.	0.00 wt.%	0.05 wt.%	0.10 wt.%	0.25 wt.%	0.5 wt.%
E [Gpa]	[24]	2.50	2.60	2.70	2.74	2.80
E [Gpa]	Present	2.50	2.53	2.57	2.68	2.86

On the basis of the fitted parameters in Table 1, the electromechanical properties of MWCNT/epoxy strip-like sensors have been computed by the present approach as shown in Table 3. Sanli et al. [9] reported that MWCNT/epoxy composites with filler contents close to the percolation threshold ($f_c \approx 0.30$ wt.%) exhibit highly nonlinear strain sensitivities. Given that linearity is a desirable feature of transducers for SHM, sensing strips doped with filler contents moderately far from the percolation threshold are used in this work, wherein the present approach is shown accurate [33]. In particular, filler mass fractions ranging from 0.50% to 1.00% have been selected with steps of 0.10%. It is noted that the piezoresistivity coefficients in Table 3 have been indicated both for compression (λ^-) and stretching (λ^+). It has been reported in the literature that MWCNT-based composites exhibit different strain-sensitivities when subjected to compression or tensile stresses, a feature that can be reproduced by the present micromechanics approach [33]. However, the differences between these piezoresistivity coefficients are small enough as observed in Table 1 that a common value is often assumed [19]. For simplicity, the piezoresistivity coefficients under tension (λ^+) are selected in the subsequent simulations.

Table 3: Effective electromechanical properties of smart MWCNT/epoxy strip-like strain sensors.

	0.50 wt.%	0.60 wt.%	0.70 wt.%	0.80 wt.%	0.90 wt.%	1.00 wt.%
λ_{11}^+	6.84	5.68	4.85	4.21	3.68	3.23
λ_{12}^+	7.99	6.83	6.01	5.36	4.83	4.38
λ_{11}^-	7.37	6.12	5.24	4.54	3.97	3.48
λ_{12}^-	8.62	7.37	6.48	5.78	5.21	4.73
λ_{44}	1.19	1.19	1.19	1.19	1.19	1.19
σ [S/m]	1.22E-02	2.05E-02	3.01E-02	4.08E-02	5.27E-02	6.56E-02
E [Gpa]	2.86	2.93	3.01	3.08	3.15	3.23
ν	0.28	0.27	0.27	0.27	0.27	0.27

4.2. Case study I: Multiple prescribed crack-like damages in 2D smart beam structures

The goal of this first case study is to investigate the performance of the proposed damage identification approach in beams with multiple prescribed crack-like damages. To this aim, 2D FE models of concrete beams equipped with MWCNT/epoxy strip-like strain sensors are developed to conduct virtual experiments. The studied beams have geometrical dimensions of length L=6 m and depth of the cross-section h=50 cm, and are subjected to a uniformly distributed load of 40 kN/m. A differential potential of 10 V is applied to the sensing strip, and the shunt resistor has an electrical resistance of 100 Ω. In order to assess the damage-induced variations in the static deflection of the beams, fully open transverse surface cracks are included in the numerical model as shown in Fig. 12. The prescribed cracks are defined with a thickness of 5 mm and a variable depth h_d, and are assumed to remain open during the analysis. In order to characterize the severity of the cracks, a non-dimensional crack depth ratio S can be defined as:

$$S = \frac{h_d}{h} \tag{27}$$

The numerical studies are conducted with the commercial FE code ANSYS v15.0 [61]. The host beams are modeled with standard plane stress elements PLANE182, considering elastic isotropic properties with Young's modulus 25 GPa and Poisson's ratio 0.2. This element type is a quadrilateral 4-nodes element with two in-plane translations per node. On the other hand, the sensing strips are modeled with piezoresistive plane elements PLANE223. This element type is a quadrilateral 4-nodes element with three degrees of freedom per node (two in-plane translations and an electric potential). Twelve equally-spaced electrodes are defined along the sensing strip to monitor the variations of the electrical resistivity. Considering that the electrodes are much more conductive than the strip, it is assumed that the electrodes can be simulated as coupling conditions of constant voltage at the

electrode sections. Additionally, in order to ensure a longitudinal electric flux, the electrodes are defined across the whole thickness of the smart strip (see Fig. 12).
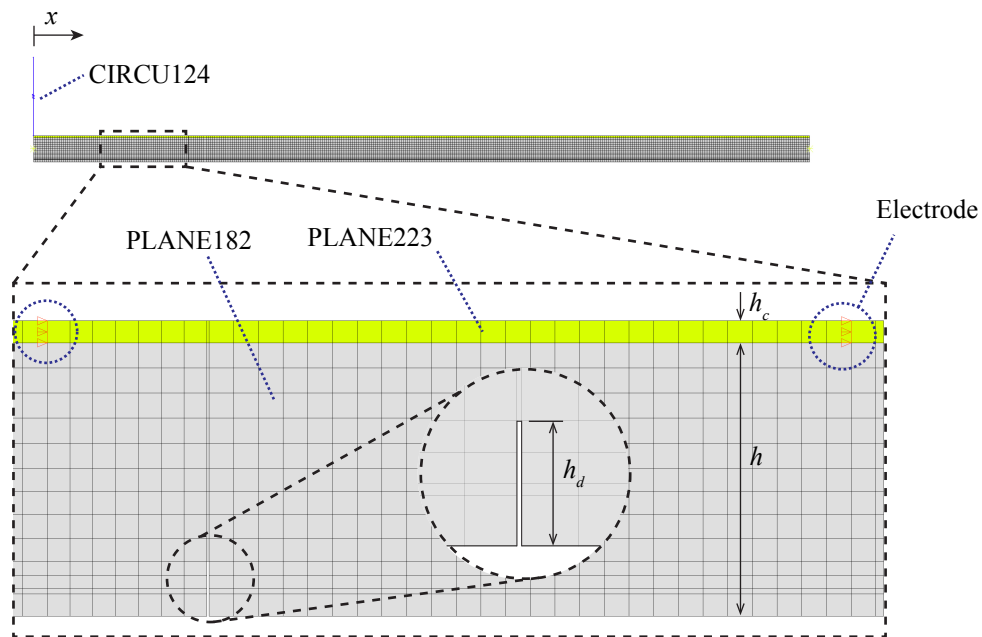

Figure 5: 2D FE model of cracked concrete beams with smart MWCNT/epoxy strip-like strain sensor.

The effect of different boundary conditions on the electrical output of the electrodes along the sensing strip is investigated in Fig. 6. In particular, Clamped-Clamped (C-C), Hinged-Hinged (H-H), and Clamped-Free (C-F) boundary conditions are considered. Firstly, Fig. 6 (a) depicts the electrical resistivity along the sensing strip for undamaged beams. Let us recall that the electrical resistivity values are attributed to the beam sections located between every two consecutive electrodes. It is observed that the output signals track the curvature of the deformed beams consistently with the different boundary conditions. Secondly, Fig. 6 (b) shows the electric current per unit of width versus the total applied vertical load. It is noted that the electric current outputted by the smart strip attached onto the C-C beam does not vary with the load. In accordance with Eq. (22), the rotations of the deformed beam at the supports for such boundary conditions are equal and, therefore, the overall electrical resistance remains unaltered. In the case of the H-H beam, the sensing strip sustains compressive strains all along the beam and, thus, the overall electrical resistance decreases while the electric current increases. With regard to the C-F beam, the sensor only sustains tensile strains and the electrical output exhibits an opposite behavior to the former case. Additionally, Fig. 7 investigates the sensitivity of smart beams with different MWCNT contents. It is clearly observed that sensing strips doped with filler contents closer to the percolation threshold ($f_c \approx 0.3$ wt.%), which exhibit larger piezoresistivity coefficients (Table 3), output larger electrical variations.
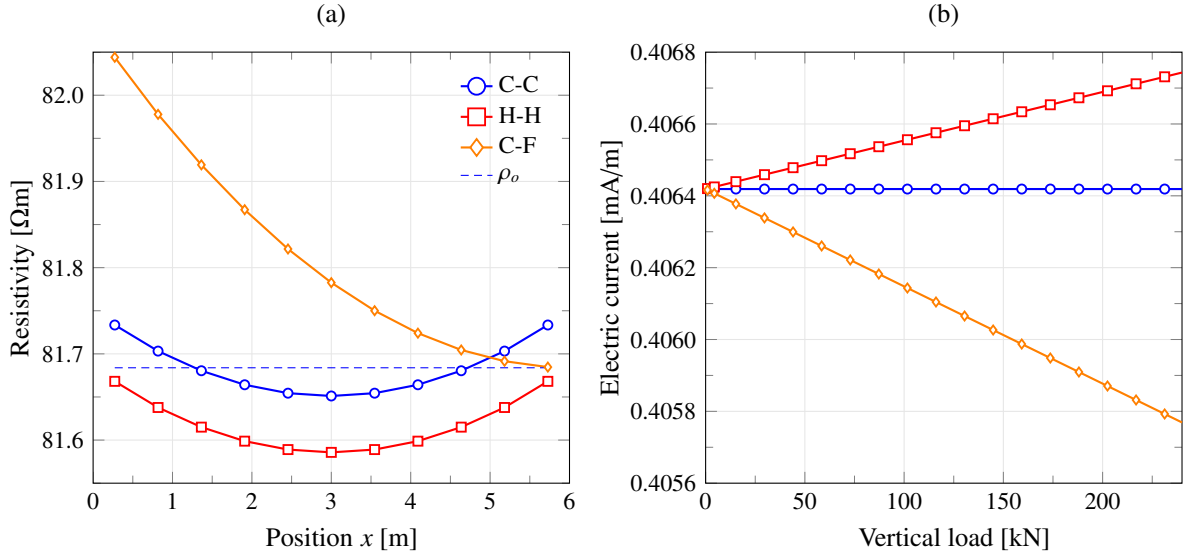
Figure 6: Electrical resistivity along the MWCNT/epoxy sensing strip attached onto a concrete beam (a), and electric current versus vertical load (b) for different boundary conditions (w_p=0.5 wt.%).
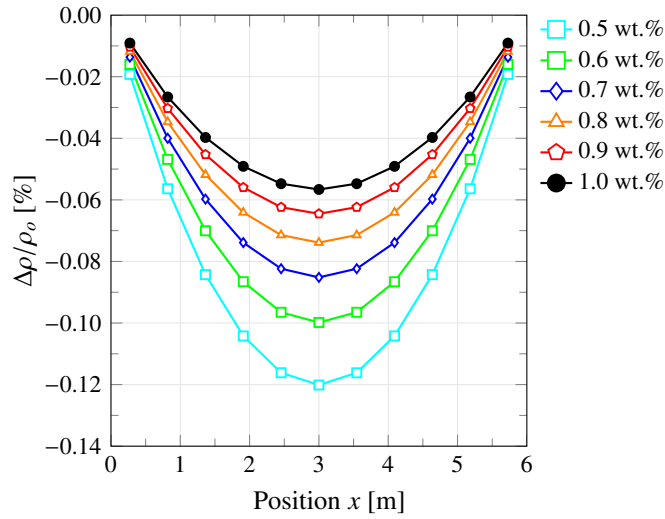

Figure 7: Relative variation of the electrical resistivity $\Delta\rho/\rho_o$ along the MWCNT/epoxy sensing strip for H-H boundary conditions with varying filler contents.

Fig. 8 investigates the effect of a single transverse crack on the electrical resistivity along the MWCNT/epoxy sensing strip for H-H boundary conditions. The cracks are located at mid-span (a) and at quarter-span (b) with increasing severity degrees S. In both cases, it is observed that the electrical resistivity locally decreases around the crack location. This is a fact that evidences the damage-induced increase in the local flexibility and, consequently, the local curvature of the beam. In addition, it is shown that increasing severity ratios S induce larger reductions in the local electrical resistivity. Therefore, it is feasible to localize the cracks and identify their severity through electrical resistance measurements and the damage identification approach presented in Section 3.

14
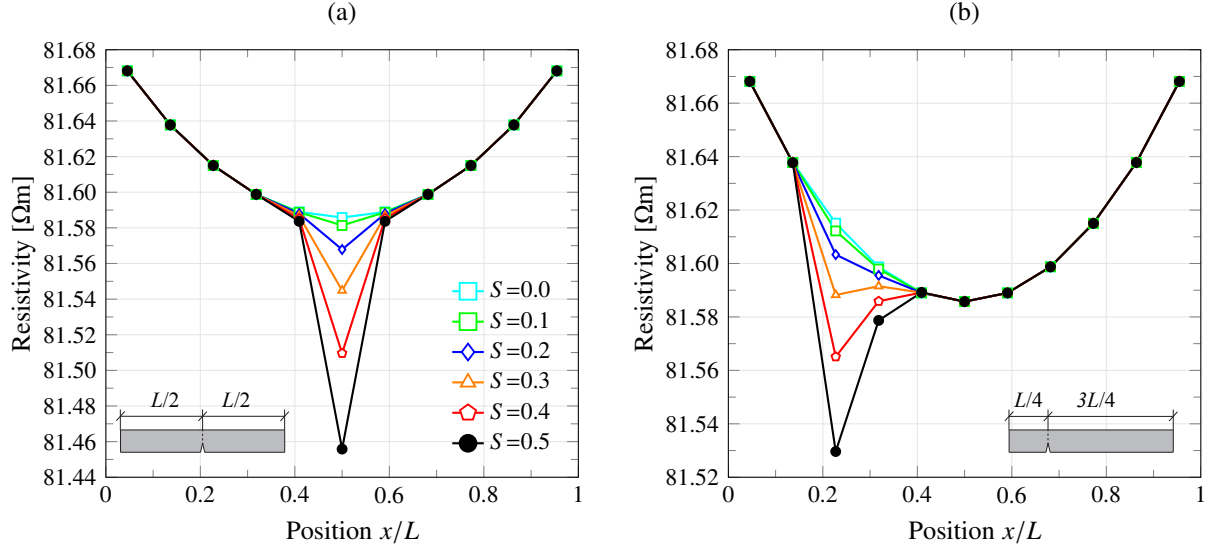
Figure 8: Electrical resistivity along the MWCNT/epoxy sensing strip for H-H boundary conditions with one single crack located at (a) half-span, and (b) at quarter-span with varying severity degrees $S = h_d/h$ (w_p=0.5 wt.%).

Figures 9, 10 and 11 present the results of the proposed damage detection approach for 2D smart beams with multiple prescribed crack-like damages. To do so, the function values $\bar{R}_{dam}$ and $\bar{R}$ in Eq. (24) are computed by the 2D FE model developed in this section and the beam model presented in Section 3, respectively, and the number of subdivisions is set to n_d=2. Firstly, Fig. 9 considers the case of one single crack located at quarter-span ($3L/4$) and two different crack depth ratios, namely S=0.1 and 0.3. It is clearly observed that damage-induced local decreases in the electrical resistivity are more prominent in the case of simply supported (H-H) beams, while the variations for fully clamped (C-C) beams are less evident. Such different behavior is ascribed to the localization of the crack which is close to the point of inflection of the deformed C-C beam. The damage intensity values calculated by the proposed damage identification approach are presented in terms of the non-dimensional damage parameter $D_k = 1 - EI_k/EI_r$. It is noted that the damage identification algorithm can correctly identify the position and severity of the crack in both cases. Secondly, Fig. 10 investigates the case of beams with two cracks located at mid-span ($L/2$) and quarter-span ($3L/4$). Two different damage configurations are studied, namely a crack depth ratio of 0.1 for both cracks, and crack depth ratios of 0.1 and 0.2 for the damages located at mid-span and quarter-span, respectively. In the case of H-H beams, it is observed that both the localization and the severity of the cracks are precisely identified. Conversely, the damage identification algorithm shows less effectiveness in the case of C-C beams. In the first configuration, including two cracks with equal crack depth ratios S=0.1, the algorithm successfully detects the crack at mid-span, whilst the one at quarter-span is not identified. However, in the second configuration, the crack depth ratio is higher in the second crack what allows the algorithm to clearly identify it. Finally, Fig. 11 analyzes the case of four cracks located at $L/5$, $2L/5$, $3L/5$ and $4L/5$. Also, two different damage configurations are defined, including crack depth ratios [0.1,0.2,0.1,0.2] and [0.2,0.1,0.1,0.2]. In the case of H-H beams, it is observed that the damage detection approach clearly identifies the position and severity of all cracks. Contrarily, in the case of C-C beams, the cracks located at $L/5$ and $3L/5$ go unnoticed by the damage identification algorithm. In this case, these cracks are very proximate to the points of inflection of the deformed beam and, therefore, the damage-induced curvature variations are minimal at these locations. This fact indicates an observability issue of those damages due to the particular boundary conditions of the beam, and the sensing principle of the proposed smart sensors (see Eq. (20)).
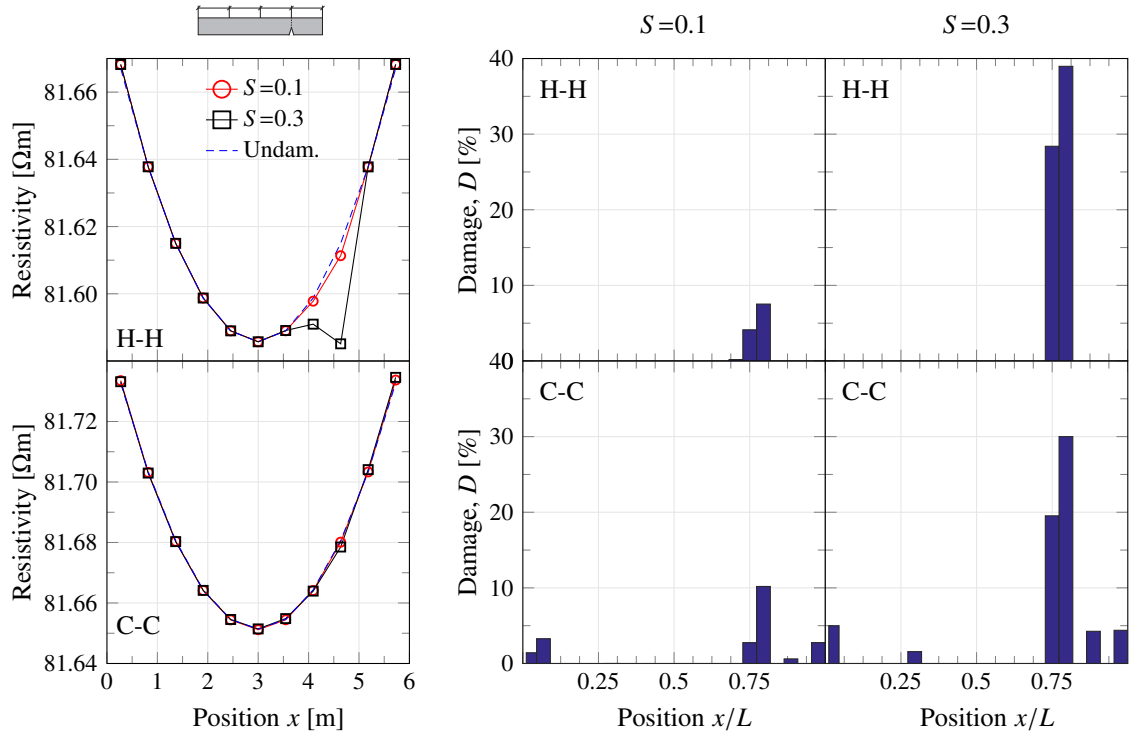
15

Figure 9: Damage identification of simply supported (H-H) and fully clamped (C-C) beams for one single transverse crack located at $3L/4$ (w_p=0.5 wt.%, n_d=2).
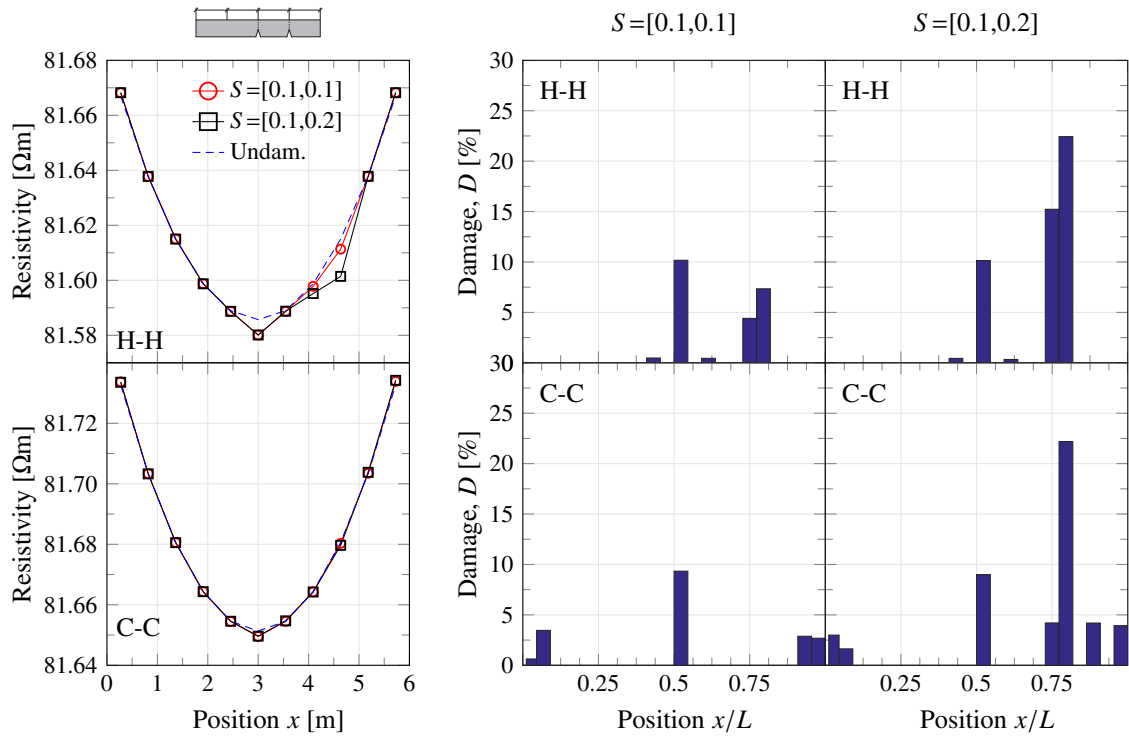

Figure 10: Damage identification of simply supported (H-H) and fully clamped (C-C) beams for two transverse cracks located at $L/2$ and $3L/4$ (w_p=0.5 wt.%, n_d=2).
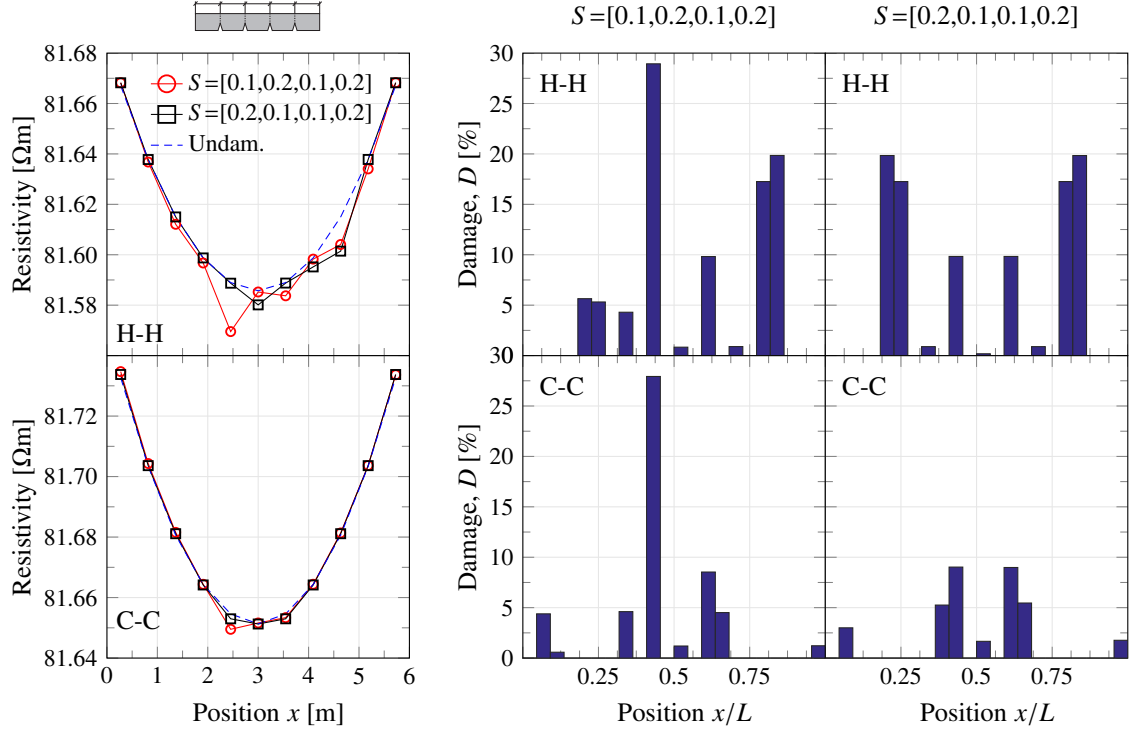
Figure 11: Damage identification of simply supported (H-H) and fully clamped (C-C) beams for four transverse cracks located at $L/5$, $2L/5$, $3L/5$ and $4L/5$ (w_p=0.5 wt.%, n_d=2).

4.3. Case study II: Smeared non-prescribed cracks in 3D smart RC beams under four-point flexural conditions

The second case study investigates the capabilities of the proposed smart MWCNT/epoxy strip-like strain sensors for damage detection in a 3D RC beam under monotonic four-point flexural conditions as shown in Fig. 12. Unlike the former case study, the damages in the RC beam are not prescribed but determined through a numerical damage model. In addition, damages are not isolated crack-like but smeared cracks in the areas subjected to tensile stresses. The studied beam is retrieved from reference [62] and has a cross-section of 25 cm width, 45 cm depth, and the beam is 400 cm long, with an effective span of 380 cm. The longitudinal reinforcement consists of two rebars of 16 mm diameter in the bottom part of the beam, and two rebars of 10 mm diameter in the upper part of the beam. Additionally, shear stirrups of 6 mm diameter are also defined along the beam with a constant spacing of 25 cm. In order to avoid stress concentration issues, 80x25x250 mm³ and 80x50x250 mm³ steel plates are arranged at the supports and loading locations, respectively. Finally, a 2.5 cm thick MWCNT/epoxy sensing strip is attached onto the upper part of the beam between the steel plates. Following the measurement scheme previously presented in Section 2, eleven equally spaced electrodes are arranged in the sensing strip defining ten sections labeled from S1 to S10. Also, a differential potential of 10 V is applied to the sensing strip and the shunt resistor has an electrical resistance of 100 Ω.
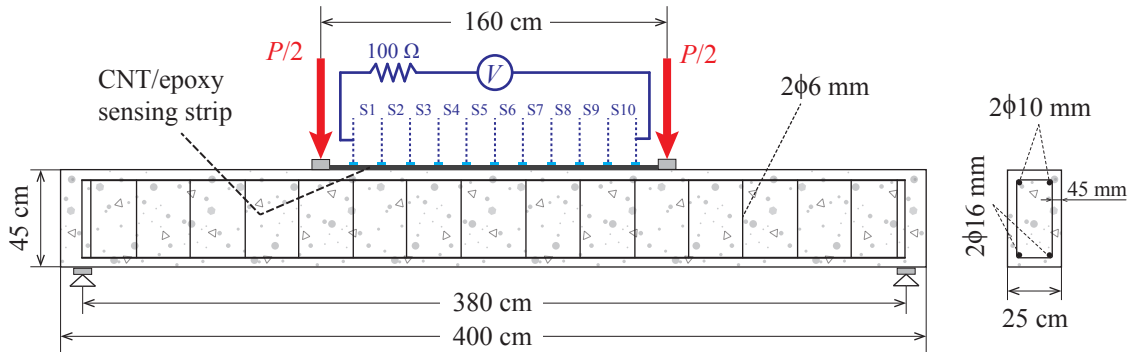

Figure 12: Loading and geometry details of RC beams with MWCNT/epoxy sensing strip.

ANSYS v15.0 [61] FE code is also chosen to model the RC beam. Concrete is modeled with the eight-nodes SOLID65 brick elements with three translational Degrees of Freedom (DOFs) per node. This element follows the Willian-Warnke yield criterion [63] to simulate failure in concrete, being capable of cracking in tension and crushing in compression. The material properties of concrete have been taken from reference [64], including a modulus of elasticity of 24.4 MPa and Poisson's ratio of 0.2. The ultimate tensile and compression strengths of concrete are taken as 3.5 MPa and 25 MPa, respectively. The compression stress-strain curve of unconfined concrete is defined according to the multilinear kinematic hardening as proposed by Kent-Park [65]. Steel bar reinforcements are idealized as uniaxial two-nodes rod elements LINK180 with three translational DOFs per node and perfect bonding is assumed between reinforcing bars and concrete. To do so, the link elements are connected between nodes of each adjacent concrete solid element. The stress-strain relationship for the steel reinforcements is defined using a bilinear isotropic hardening model with Young's modulus 200 GPa, Poisson's ratio 0.3, yield stress 400 MPa, and hardening stiffness 20 MPa. The steel supports are modeled with standard SOLID185 brick elements and linearly elastic isotropic properties with Young's modulus 210 GPa and Poisson's ratio 0.3. The MWCNT/epoxy smart strip is modeled with linear piezoresistive SOLID226 elements. These solid elements have twenty nodes and four DOFs per node (three translations and an electric potential), and their electromechanical properties are taken from Table 3. Finally, The shunt resistor is modeled with the general two-nodes circuit element CIRCU124.

Fig. 13 depicts the applied load P versus the vertical deflection at mid-span, respectively. It is observed in this figure that the first crack appears at around P=60 kN. Then, the slope of the curve decreases and remains approximately constant until P=110 kN, where yielding of the bottom steel reinforcements start. This behavior comprises three well-differentiated regions, namely the elastic uncracked region I, the elastic cracked region II, and the plastic cracked region III. In order to investigate the ability of the MWCNT/epoxy sensing strip to detect damages, three load cases are selected attending to the three identified regions, namely LC1 (P=31.18 kN, δ=0.05 cm), LC2 (P=74.76 kN, δ=0.57 cm) and LC3 (P=117.50 kN, δ=1.28 cm).
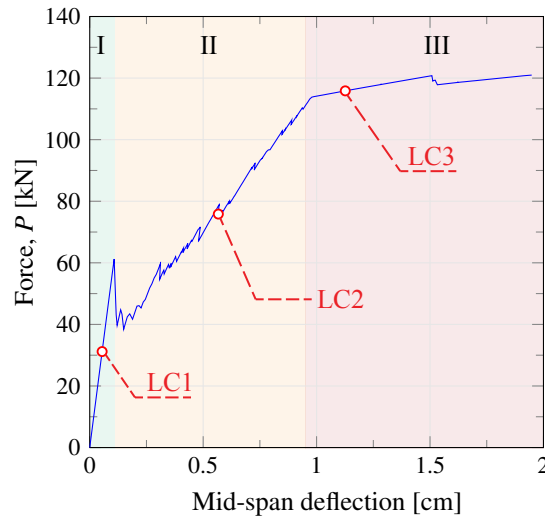

Figure 13: Applied load versus vertical deflection at mid-span for RC beam with MWCNT/epoxy sensing strip under four-point flexural conditions, with key behavior stages of reinforced concrete (I, II and III) annotated (w_p=0.5 wt.%).

The crack pattern at each load step is monitored during the simulations. Fig. 14 shows the crack pattern developed in the RC beam at two different simulation steps. Cracks at the integration points are represented with circle outlines in the plane of the cracks. It can be observed in this figure that flexural cracks occur in the mid-span and are followed by diagonal shear cracks near the supports. Moreover, crushing of the upper section of the RC beam in the loading span follows the yielding of the bottom reinforcing rebars. Finally, Fig. 15 shows the vertical displacement (a) and longitudinal electric field through the smart strip (b) at the end of the loading.
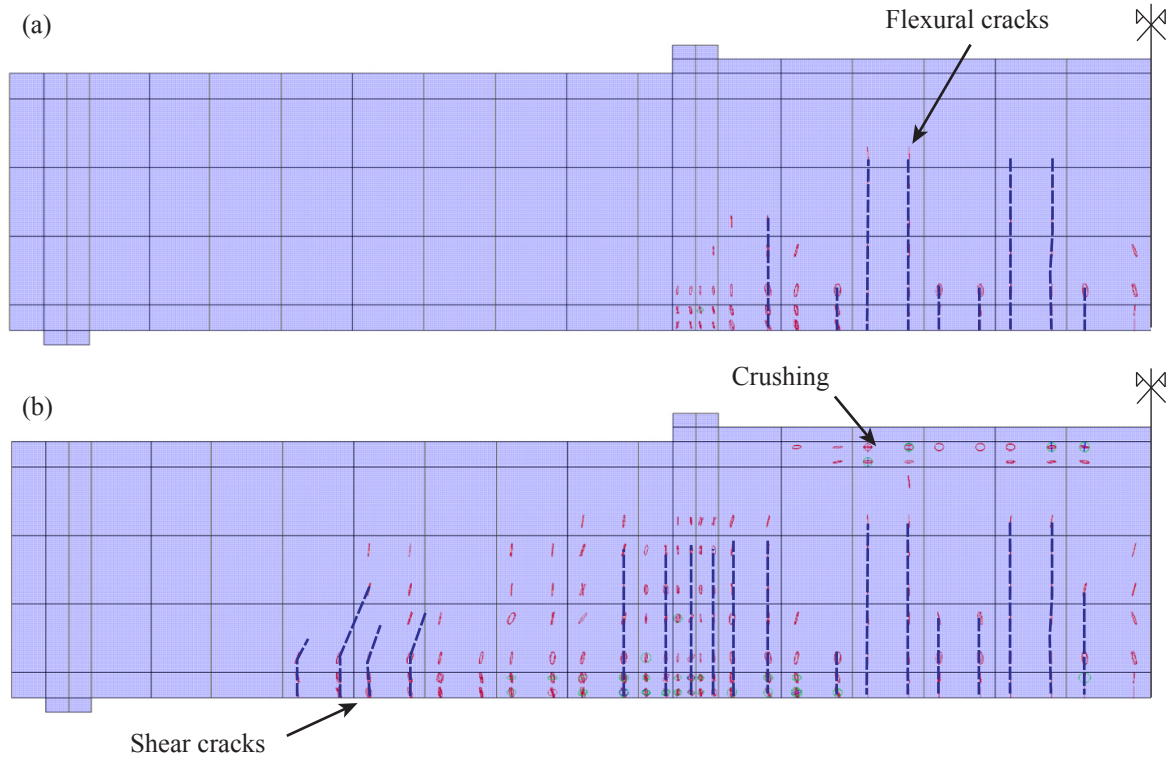
18

Figure 14: Numerical evolution of crack pattern of RC beam with MWCNT/epoxy sensing strip (P=70 kN (a), and $P = 119$ kN (b), w_p=0.5 wt.%). The blue dashed lines have been included a posteriori to remark the crack orientations.
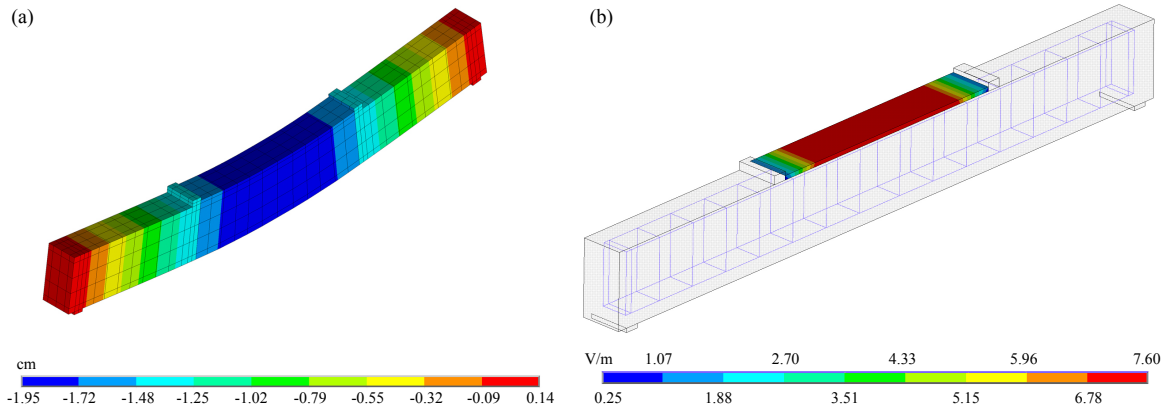

Figure 15: Vertical displacements (a) and longitudinal electric field through the MWCNT/epoxy sensing strip (b) at the end of the loading ($P = 119$ kN, w_p=0.5 wt.%).

In this study, two different electrodes layouts have been analyzed as shown in Fig. 16, namely superficial and full penetration electrodes. In the first configuration, it is assumed that electrodes are simply attached onto the upper surface of the sensor, while in the second one the electrodes completely penetrate the cross-section of the strip. In the numerical model, the first case is modeled by coupling the electric potentials of the nodes located in the upper part of the strip, whilst the potentials of all the nodes on the cross-section of the sensor are coupled in the second case. Following these two electrodes layouts, Fig. 17 depicts the electrical resistivity calculated along the length L_s of the MWCNT/epoxy sensing strip under the three load cases previously defined in Fig. 13. Interestingly, it is observed that the definition of superficial electrodes induces additional contact resistances, which are especially notable in the extreme sections. These results are in agreement with previously reported experimental results (see e.g. Fig. 6 in [19]), and such effect is ascribed to the alteration of the longitudinal electric flux due to the presence of electrodes in the upper part of the strip. Conversely, the definition of electrodes with full penetration eliminates this effect and makes the electric flux become perfectly longitudinal. In this case, it is clearly

observed that the electrical resistivity follows an horizontal line in the undamaged loading condition (LC1), a response that is expected from the constant bending efforts sustained by the beam in the loading span. Nonetheless, when higher load levels are considered, i.e. LC2 and LC3, it is noted that the electrical resistivity ceases being constant along the sensor, a fact that evidences the presence of structural damage. The electrical currents flowing through the 0.5 wt.% MWCNT/epoxy sensing strips with superficial and full penetration electrodes layouts versus the midspan displacements are depicted in Fig. 18. Given that the upper part of the beam sustains increasing compressions under increasing flexural loadings, it is noted that the electrical current exhibits an increasing trend in both cases and, therefore, the overall electrical resistance of the strip decreases. As a result of the artificial contact resistances induced by the superficial electrodes layout, the electrical current in this case is slightly lower than that with full penetration electrodes arrangement. Although some correlations can be observed between the electrical current and the damage process in the RC beam, it is necessary to closely inspect the voltage drops along the strip and local disturbances in its internal resistance to clearly identify the damages as shown hereafter.
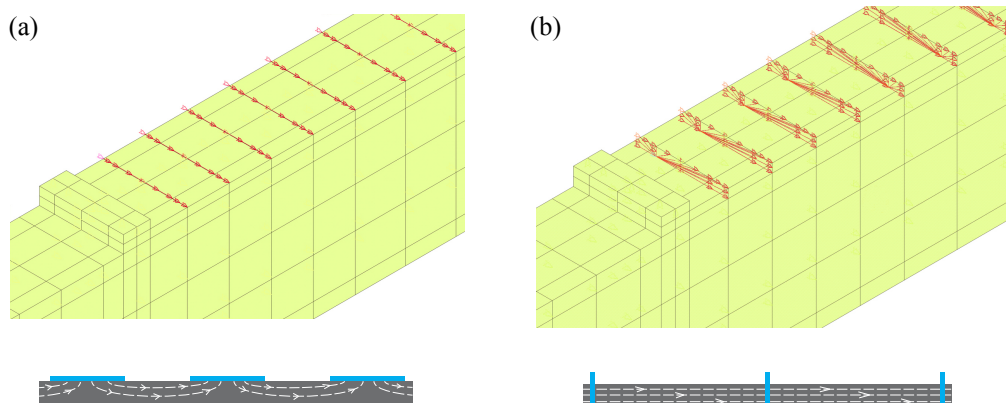

Figure 16: Electrodes layouts: (a) superficial electrodes and (b) full penetration electrodes.
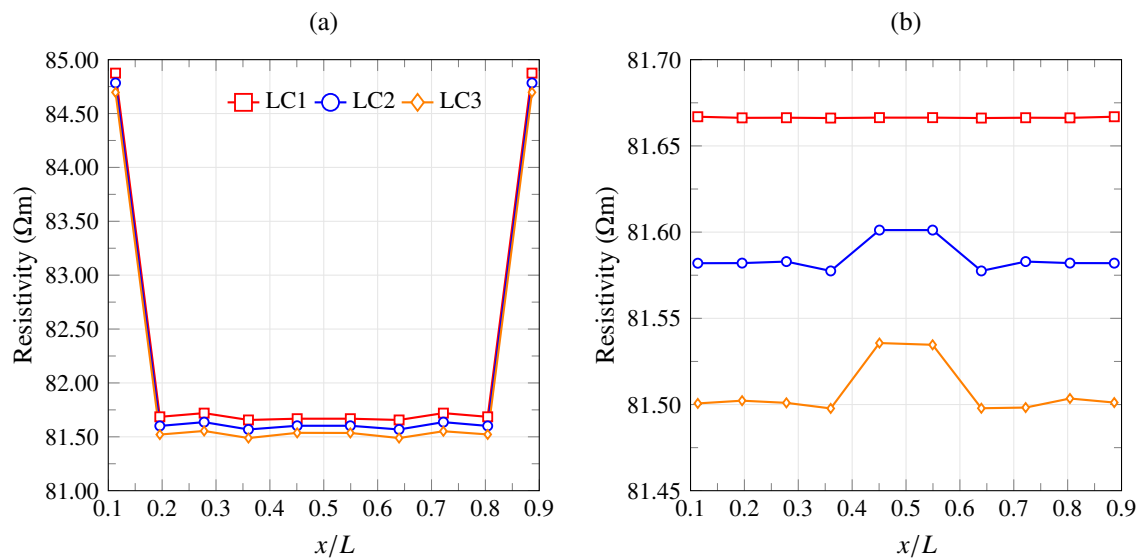

Figure 17: Electrical resistivity along the MWCNT/epoxy sensing strip with superficial electrodes (a) and full penetration electrodes (b) (w_p=0.5 wt.%).
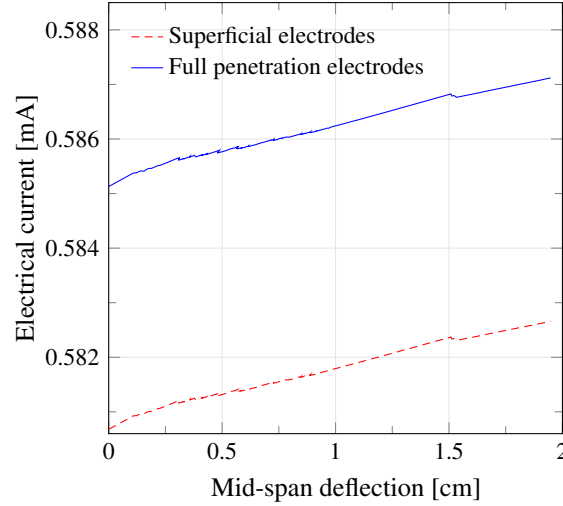
Figure 18: Electrical current versus vertical deflection at mid-span for RC beam with MWCNT/epoxy sensing strip with superficial electrodes (a) and full penetration electrodes (b) (w_p=0.5 wt.%).

Fig. 19 represents the load P versus the electrical resistivity at different sections of the sensing strip for both superficial and full penetration electrodes layouts. In the case of superficial electrodes in Fig. 19 (a), the results computed in the first section S1 have been omitted for clarity purposes. Let us recall that, as previously shown in Fig. 17, the artificial contact resistance induced by superficial electrodes layouts substantially rises the electrical resistivity in the extreme sections of the sensor. It is observed in this case that the curves do not coincide for loading levels before cracking, a fact that evidences that superficial electrodes layouts also induce artificial contact resistances all along the strip. Conversely, in the case of full penetration electrodes layout in Fig. 19 (b), the electrical resistivities calculated in the different sections of the sensor overlap until the appearance of the first cracks. Nonetheless, the cracking initiation is clearly registered in both configurations as a sudden change in the slopes of the curves and, therefore, it is concluded that both setups show capabilities for damage detection applications.
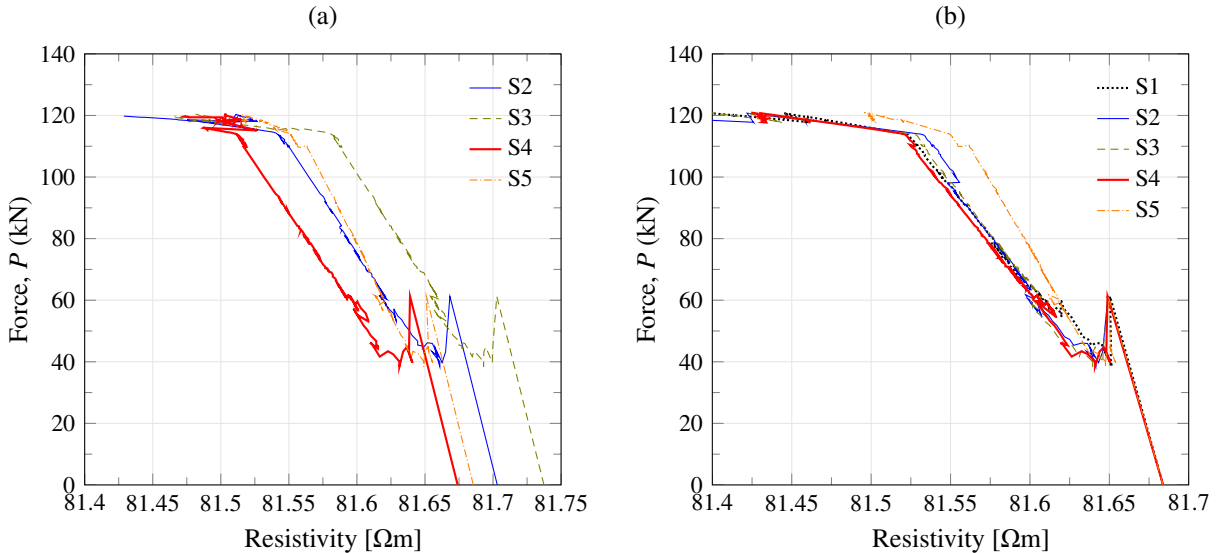

Figure 19: Force P versus the electrical resistivity at different sections of the smart MWCNT/epoxy strip-like strain sensor for (a) superficial and (b) full penetration electrodes layouts (w_p=0.5 wt. %).

Fig. 20 investigates the apparent variation of the electrical resistivity at sections S1 (a) and S5 (b) of the smart MWCNT/epoxy strip doped with different filler contents. Firstly, it is observed that, in accordance with the results previously shown in Fig. 7, filler contents closer to the percolation threshold ($f_c \approx 0.3$ wt.%) lead to higher sensitivities. Interestingly, it is observed that such differences are considerably larger in the elastic cracked region (region II). This remark is of high practical interest because, in normal conditions, most RC structures

usually operate within this range. In order to further the analysis on the electrodes layouts, solid and dashed lines depict the results calculated with superficial and full penetration electrodes layouts, respectively. In the first section S1, the electrical outputs calculated by the two electrodes arrangements are not coincident, with slightly higher discrepancies in the elastic cracked region. Contrarily, these differences are minimal in the section S5. As a conclusion, it is extracted that the artificial contact resistances induced by superficial electrodes layouts are more determinant in the extreme sections, while these substantially decrease in sections far from the extremes.
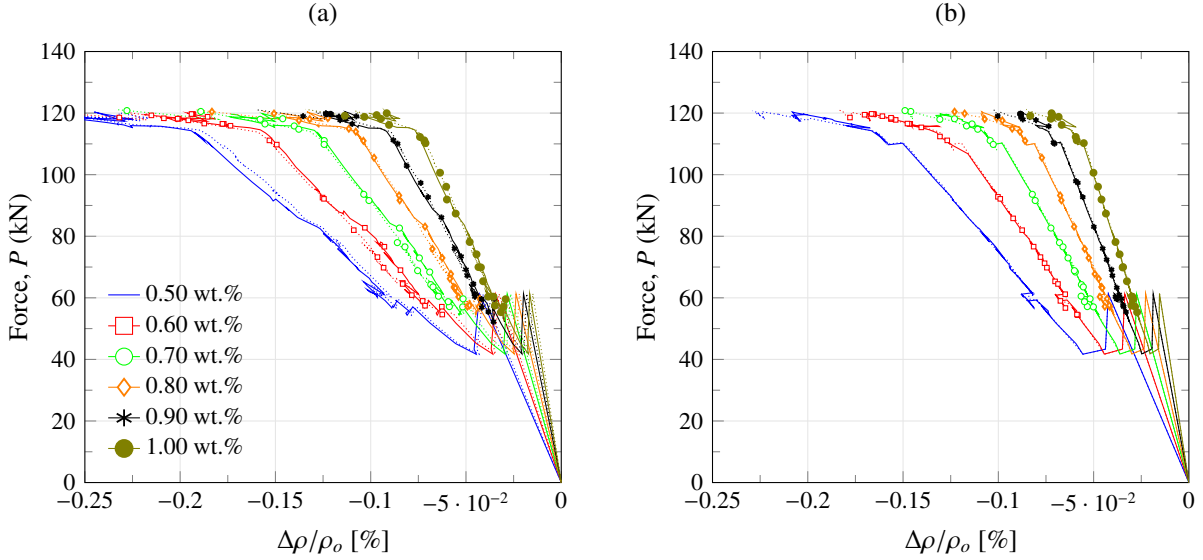

Figure 20: Force P versus the apparent variation of the electrical resistivity at sections S1 (a) and S5 (b) of the smart MWCNT/epoxy strip for different filler contents. Solid and dashed lines stand for superficial and full penetration electrodes layouts, respectively.

Finally, the results of the damage identification algorithm previously introduced in Section 3 are furnished in Fig. 21. In the analysis, both superficial and full penetration electrodes layouts are considered, as well as the three different load cases defined by LC1, LC2 and LC3. In this case, the function values $\overline{R}_{dam}$ and $\overline{R}$ in Eq. (24) are computed by the 3D FE model developed in this section and the beam model presented in Section 3, respectively, and the number of subdivisions has been set to n_d=1. Firstly, none of the electrodes layouts detect damage in the loading case LC1, therefore no false positive errors are committed. Secondly, the presence of a moderate level of damage in LC2 is only detected by the smart strip with full penetration electrode layout. In this case, the damage detection approach furnishes the presence of moderate damages. Furthermore, damage concentrations are found around $Ls/3$ and $2L_s/3$, what is consistent with the crack patterns previously shown in Fig. 14. Conversely, it is noted that the sensing strip with superficial electrodes fails to detect the damage. Thirdly, the high level of structural damage in LC3 is easily detected by the smart strips with both electrodes layouts. In both cases, smeared cracks are detected by the strips' sections close to the load application points, as well as damage concentrations around $Ls/3$ and $2L_s/3$. The damage severity values calculated through the sensor with superficial electrodes are lower than those identified with the one with full penetration electrodes layout. Moreover, in the former case, the results indicate concentration of damages at the mid-span of the RC beam, what is inconsistent with the simulation results. Hence, it is concluded that smart strips with superficial electrodes layouts can be used for damage detection of moderate to high levels of damage. Nevertheless, the presence of artificial contact resistances stemming from the electric boundary conditions limits the effectiveness of such smart strips in damage localization and quantification, so, in practical applications, a special care must be posed on the electrodes themselves.
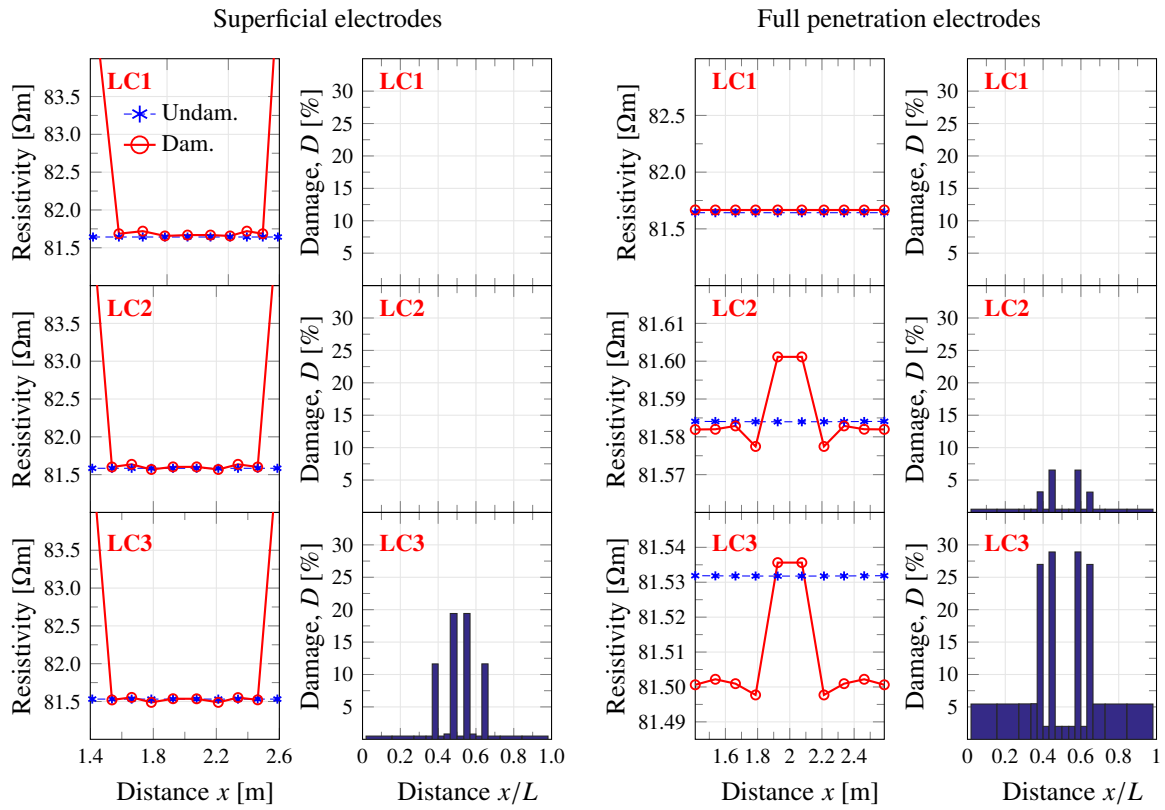
Superficial electrodes

Full penetration electrodes

Figure 21: Damage identification of RC beams with CNY/epoxy sensing skins under four-point flexural loading conditions (w_p=0.5 wt.%, LC1: P=31.18 kN, δ=0.05 cm; LC2: P=76.00 kN, δ=0.56 cm; LC3: P=118.13 kN, δ=1.39 cm).

5. Conclusions

This work has presented a theoretical study on smart MWCNT/epoxy strip-like strain sensors for damage detection/localization/quantification in beam structures. A feasible measurement layout based on the acquisition of the voltage drops along multisectioned smart strips has been shown capable of tracking the strain distribution along the host beams. The electromechanical modeling of MWCNT/epoxy strips has been conducted by a micromechanics-based FE modeling. The micromechanical variables utilized in the numerical simulations have been obtained by fitting experimental data retrieved from the literature. Furthermore, a simple and fast damage identification algorithm through a model updating approach has been presented. To do so, an Euler-Bernoulli model for beams equipped with a smart MWCNT/epoxy strip has been developed. Finally, two case studies have been presented including: a 2D concrete beam with multiple prescribed crack-like damages, and a 3D RC beam under four-point flexural conditions.

The key findings of this work can be summarized as follows:

- Multisectioned smart MWCNT/epoxy strips have been shown feasible for tracking the strain distribution along monitored beams. In particular, it has been demonstrated that smart strips attached onto beam structures essentially behave as distributed curvature sensors.

- Crack-like damages induce local variations of the beams' flexibility and, therefore, the presence of damages manifests as local disturbances in the electrical output of MWCNT/epoxy strips.

- The proposed damage identification approach has been proved efficient in the case of multiple prescribed crack-like damages. The numerical results have demonstrated the ability of the proposed approach to localize and quantify the severity of multiple damages. In addition, discussion has been provided concerning the observability issues related to damages located at the inflection points of the deflection lines of the monitored beams.

- Two different electrodes layouts have been investigated including: superficial electrodes, and full penetration electrodes. It has been numerically demonstrated that superficial electrodes infer artificial contact resistances in the sensing strips, with a large influence on the extreme sections, as it was experimentally observed in previous work in the literature, but never explained before.

- It has been reported that smart MWCNT/epoxy strips doped with filler contents closer to the percolation threshold exhibit higher sensitivities, especially in the elastic cracked region of RC beams.

- The proposed damage identification approach has been shown suitable for damage detection of non-prescribed diffuse cracks. Smart strips with full penetration electrodes layouts have been reported efficient to localize and quantity smeared cracks in a RC beam under monotonic four-point flexural conditions. Conversely, the artificial contact resistances induced by superficial electrodes arrangements have been shown to hinder the detection of moderate damages, as well as the accurate localization of damages.

References

[1] B. Mather, Concrete durability, Cement and Concrete Composites 26 (2004) 3–4.

[2] B. Han, J. Ou, Embedded piezoresistive cement-based stress/strain sensor, Sensors and Actuators A: Physical 138 (2007) 294–298.

[3] M. Enckell, B. Glisic, F. Myrvoll, B. Bergstrand, Evaluation of a large-scale bridge strain, temperature and crack monitoring with distributed fibre optic sensors, Journal of Civil Structural Health Monitoring 1 (2011) 37–46.

[4] B. Glisic, D. Inaudi, Distributed fiber-optic sensing and integrity monitoring, Transportation Research Record: Journal of the Transportation Research Board 2150 (2010) 96–102.

[5] O. Galao, F. Baeza, E. Zornoza, P. Garcés, Strain and damage sensing properties on multifunctional cement composites with CNF admixture, Cement and concrete composites 46 (2014) 90–98.

[6] S. P. Shah, M. Konsta-Gdoutos, Z. Metaxa, P. Mondal, Nanoscale modification of cementitious materials, in: Nanotechnology in Construction 3, Springer, 2009, pp. 125–130.

[7] B. Han, S. Ding, X. Yu, Intrinsic self-sensing concrete and structures: A review, Measurement 59 (2015) 110–128.

[8] R. Pilawka, S. Paszkiewicz, Z. Rosłaniec, Epoxy composites with carbon nanotubes, Advances in Manufacturing Science and Technology 36 (2012) 67–79.

[9] A. Sanli, C. Müller, O. Kanoun, C. Elibol, M. F. X. Wagner, Piezoresistive characterization of multi-walled carbon nanotube-epoxy based flexible strain sensitive films by impedance spectroscopy, Composites Science and Technology 122 (2016) 18–26.

[10] A. Downey, A. D'Alessandro, S. Laflamme, F. Ubertini, Smart bricks for strain sensing and crack detection in masonry structures, Smart Materials and Structures 27 (2017) 015009.

[11] A. B. Flatau, K. P. Chong, Dynamic smart material and structural systems, Engineering Structures 24 (2002) 261–270.

[12] S. Hurlebaus, L. Gaul, Smart structure dynamics, Mechanical Systems and Signal Processing 20 (2006) 255–281.

[13] M. Hallaji, P. G. Mohammad, A new sensing skin for qualitative damage detection in concrete elements: Rapid difference imaging with electrical resistance tomography, NDT & E International 68 (2014) 13–21.

[14] Y. Yao, B. Glisic, Detection of steel fatigue cracks with strain sensing sheets based on large area electronics, Sensors 15 (2015) 8088–8108.

[15] S. Laflamme, M. Kollosche, J. J. Connor, G. Kofod, Soft capacitive sensor for structural health monitoring of large-scale systems, Structural Control and Health Monitoring 19 (2012) 70–81.

[16] A. Meoni, A. D'Alessandro, A. Downey, E. García-Macías, M. Rallini, A. L. Materazzi, L. Torre, S. Laflamme, R. Castro-Triguero, F. Ubertini, An experimental study on static and dynamic strain sensitivity of smart concrete sensors doped with carbon nanotubes for SHM of large structures, Sensors 18 (2018) 831.

[17] T. Schumacher, E. T. Thostenson, Development of structural carbon nanotube–based sensing composites for concrete structures, Journal of Intelligent Material Systems and Structures 25(11) (2013) 1331–1339.

[18] R. N. Howser, H. B. Dhonde, Y. L. Mo, Self-sensing of carbon nanofiber concrete columns subjected to reversed cyclic loading, Smart Materials and Structures 20 (2011) 085031.

[19] A. Downey, A. D'Alessandro, M. Baquera, E. García-Macías, D. Rolfes, F. Ubertini, S. Laflamme, R. Castro-Triguero, Damage detection, localization and quantification in conductive smart concrete structures using a resistor mesh model, Engineering Structures 148 (2017) 924–935.

[20] A. H. Korayem, N. Tourani, M. Zakertabrizi, A. M. Sabziparvar, W. H. Duan, A review of dispersion of nanoparticles in cementitious matrices: Nanoparticle geometry perspective, Construction and Building Materials 153 (2017) 346–357.

[21] F. Naeem, H. K. Lee, H. K. Kim, I. W. Nam, Flexural stress and crack sensing capabilities of MWNT/cement composites, Composite Structures 175 (2017) 86–100.

[22] I. Kang, M. J. Schulz, J. H. Kim, V. Shanov, D. Shi, A carbon nanotube strain sensor for structural health monitoring, Smart Materials and Structures 15 (2006) 737–748.

[23] J. N. Coleman, U. Khan, W. J. Blau, Y. K. Gunko, Small but strong: a review of the mechanical properties of carbon nanotube–polymer composites, Carbon 44 (2006) 1624–1652.

[24] F. Vahedi, H. R. Shahverdi, M. M. Shokrieh, M. Esmkhani, Effects of carbon nanotube content on the mechanical and electrical properties of epoxy-based composites, New Carbon Materials 29 (2014) 419–425.

[25] R. Rafiee, R. M. Moghadam, On the modeling of carbon nanotubes: A critical review, Composites Part B: Engineering 56 (2014) 435–449.

[26] A. K. Gupta, S. P. Harsha, Analysis of mechanical properties of carbon nanotube reinforced polymer composites using multi-scale finite element modeling approach, Composites Part B: Engineering 95 (2016) 172–178.

[27] Y. Benveniste, T. Miloh, Imperfect soft and stiff interfaces in two-dimensional elasticity, Mechanics of materials 33 (2001) 309–323.

[28] M. Rouhi, M. Rais-Rohani, Modeling and probabilistic design optimization of a nanofiber-enhanced composite cylinder for buckling, Composite Structures 95 (2013) 346–353.

[29] W. Xu, F. Wu, Y. Jiao, M. Liu, A general micromechanical framework of effective moduli for the design of nonspherical nano-and micro-particle reinforced composites with interface properties, Materials & Design 127 (2017) 162–172.

[30] S. Wen, D. D. L. Chung, Double percolation in the electrical conduction in carbon fiber reinforced cement-based materials, Carbon 45 (2007) 263–267.

[31] L. Chang, K. Friedrich, L. Ye, P. Toro, Evaluation and visualization of the percolating networks in multi-wall carbon nanotube/epoxy composites, Journal of materials science 44 (2009) 4003–4012.

[32] C. Feng, L. Jiang, Investigation of uniaxial stretching effects on the electrical conductivity of CNT-polymer nanocomposites, Journal of Physics D: Applied Physics 47 (2014) 405103.

[33] E. García-Macías, A. D'Alessandro, R. Castro-Triguero, D. Pérez-Mira, F. Ubertini, Micromechanics modeling of the uniaxial strain-sensing property of carbon nanotube cement-matrix composites for SHM applications, Composite Structures 163 (2017) 195–215.

[34] F. Deng, Q. S. Zheng, An analytical model of effective electrical conductivity of carbon nanotube composites, Applied Physics Letters 92 (2008) 071902.

[35] T. Takeda, Y. Shindo, Y. Kuronuma, F. Narita, Modeling and characterization of the electrical conductivity of carbon nanotube-based polymer composites, Polymer 52 (2011) 3852–3856.

[36] C. Feng, L. Jiang, Micromechanics modeling of the electrical conductivity of carbon nanotube (CNT)–polymer nanocomposites, Composites Part A: Applied Science and Manufacturing 47 (2013) 143–149.

[37] L. Y. Alamusi, N. Hu, Numerical simulations on piezoresistivity of CNT/polymer based nanocomposites, Computers Materials & Continua 20 (2010) 101–117.

[38] T. Tallman, K. W. Wang, An arbitrary strains carbon nanotube composite piezoresistivity model for finite element integration, Applied Physics Letters 102 (2013) 011909.

[39] C. Feng, L. Jiang, Micromechanics modeling of bi-axial stretching effects on the electrical conductivity of CNT-polymer composites, International Journal of Applied Mechanics 7 (2015) 1550005.

[40] E. García-Macías, R. Castro-Triguero, A. Sáez, F. Ubertini, 3D mixed micromechanics-FEM modeling of piezoresistive carbon nanotube smart concrete., Computer Methods in Applied Mechanics and Engineering, *In press* (2018).

[41] W. K. Hsu, V. Kotzeva, P. C. P. Watts, G. Z. Chen, Circuit elements in carbon nanotube-polymer composites, Carbon 42 (2004) 1707–1712.

[42] A. Alizadeh Sahraei, M. Ayati, M. Baniassadi, D. Rodrigue, M. Baghani, Y. Abdi, AC and DC electrical behavior of MWCNT/epoxy nanocomposite near percolation threshold: Equivalent circuits and percolation limits, Journal of Applied Physics 123 (2018) 105109.

[43] A. Downey, A. D'Alessandro, F. Ubertini, S. Laflamme, R. Geiger, Biphasic DC measurement approach for enhanced measurement stability and multi-channel sampling of self-sensing multi-functional structural materials doped with carbon-based additives, Smart Materials and Structures 26 (2017) 065008.

[44] F. Deng, K. J. Van Vliet, Prediction of elastic properties for polymer-particle nanocomposites exhibiting an interphase, Nanotechnology 22 (2011) 165703.

[45] M. Hori, S. Nemat-Nasser, Double-inclusion model and overall moduli of multi-phase composites, Mechanics of Materials 14 (1993) 189–206.

[46] W. Xu, H. Ma, S. Ji, H. Chen, Analytical effective elastic properties of particulate composites with soft interfaces around anisotropic particles, Composites Science and Technology 129 (2016) 10–18.

[47] J. G. Simmons, Generalized formula for the electric tunnel effect between similar electrodes separated by a thin insulating film, Journal of Applied Physics 34 (1963) 1793–1803.

[48] E. García-Macías, A. D'Alessandro, R. Castro-Triguero, D. Pérez-Mira, F. Ubertini, Micromechanics modeling of the electrical conductivity of carbon nanotube cement-matrix composites, Composites Part B: Engineering 108 (2017) 451–469.

[49] G. Odegard, T. Gates, Constitutive modeling of nanotube/polymer composites with various nanotube orientation, in: 2002 SEM Annual Conference on Experimental and Applied Mechanincs.

[50] G. D. Seidel, D. C. Lagoudas, A micromechanics model for the electrical conductivity of nanotube-polymer nanocomposites, Journal of Composite Materials 43 (2009) 917–941.

[51] N. Hu, H. Fukunaga, S. Atobe, Y. Liu, J. Li, Piezoresistive strain sensors made from carbon nanotubes based polymer nanocomposites, Sensors 11 (2011) 10691–10723.

[52] T. Komori, K. Makishima, Numbers of fiber-to-fiber contacts in general fiber assemblies, Textile Research Journal 47 (1977) 13–17.

[53] Y. Kuronuma, T. Takeda, Y. Shindo, F. Narita, Z. Wei, Electrical resistance-based strain sensing in carbon nanotube/polymer composites under tension: analytical modeling and experiments, Composites Science and Technology 72 (2012) 1678–1682.

[54] A. Sobha, S. K. Narayanankutty, Improved strain sensing property of functionalised multiwalled carbon nanotube/polyaniline composites in TPU matrix, Sensors and Actuators A: Physical 233 (2015) 98–107.

[55] G. K. Johns, Modeling piezoresistivity in silicon and polysilicon, Journal of Applied Engineering Mathematics April 2 (2006) 1–5.

[56] V. A. Morozov, Methods for solving incorrectly posed problems, Springer Science & Business Media, 2012.

[57] B. Titurus, M. I. Friswell, Regularization in model updating, International Journal for numerical methods in engineering 75 (2008) 440–478.

[58] C. Laurent, E. Flahaut, A. Peigney, The weight and density of carbon nanotubes versus the number of walls and diameter, Carbon 48 (2010) 2994–2996.

[59] M. M. Shokrieh, M. Esmkhani, Z. Shokrieh, Z. Zhao, Stiffness prediction of graphene nanoplatelet/epoxy nanocomposites by a combined molecular dynamics-micromechanics method, Computational Materials Science 92 (2014) 444–450.

[60] M. F. Yu, O. Lourie, M. J. Dyer, K. Moloni, T. F. Kelly, R. S. Ruoff, Strength and breaking mechanism of multiwalled carbon nanotubes under tensile load, Science 287 (2000) 637–640.

[61] Structural analysis guide, Release 15.0, ANSYS Inc, Cannonsburg, PA (2014).

[62] N. S. Badiger, K. M. Malipatil, Parametric Study on Reinforced Concrete Beam using ANSYS, Civil and Environmental Research 6 (2014) 88–94.

[63] K. J. William, E. D. Warnke, Constitutive model for the triaxial behavior of concrete, volume 19, ISMES, Bergamo, Italy, pp. 174–186.

[64] D. Tjitradi, E. Eliatun, S. Taufik, 3D ANSYS numerical modeling of reinforced concrete beam behavior under different collapsed mechanisms, International Journal of Mechanics and Applications 7 (2017) 14–23.

[65] D. C. Kent, R. Park, Flexural members with confined concrete, Journal of the Structural Division (1971).